J. Fluid Mech. (2026), *vol.* 1031, A49, doi:10.1017/jfm.2026.11329

Distinguished regimes of 2-D internal gravity wave turbulence

Vincent Labarre[1,2,3] **and Michal Shavit**[4]

[1]Université Côte d'Azur, Observatoire de la Côte d'Azur, CNRS, Laboratoire Lagrange, Boulevard de l'Observatoire CS 34229, CEDEX 4, Nice F 06304, France

[2]LadHyX, CNRS, École polytechnique, Institut polytechnique de Paris, 91120, Palaiseau, France

[3]Aix-Marseille University, CNRS, Centrale Med, IRPHE, Marseille, France

[4]Courant Institute of Mathematical Sciences, New York University, NY 10012, USA

Corresponding authors: Vincent Labarre, vincent.labarre@univ-amu.fr; Michal Shavit, ms14479@nyu.edu

(Received 12 February 2025; revised 13 February 2026; accepted 14 February 2026)

Using weak wave turbulence theory analysis, we distinguish three main regimes for two-dimensional (2-D) stratified fluids in the dimensionless parameter space defined by the Froude number and the Reynolds number: discrete wave turbulence, weak wave turbulence and strong nonlinear interaction. These regimes are investigated using direct numerical simulation (DNS) of the 2-D Boussinesq equations with shear modes removed. In the weak wave turbulence regime, excluding slow frequencies, we observe a spectrum that aligns with recent predictions from kinetic theory. This finding represents the first DNS-based confirmation of wave turbulence theory for internal gravity waves. At strong stratification, in both the weak and strong interaction regimes, we observe the formation of layers accompanied by spectral peaks at low discrete frequencies. We attribute this layering to an inverse kinetic-energy transfer in combination with discrete wave–wave interactions at large scales. This analysis allows us to predict the layer thickness and typical flow velocity in terms of the control parameters.

Key words: stratified turbulence, wave-turbulence interactions, wave breaking

1. Introduction

Internal gravity waves propagating within stably stratified fluids are ubiquitous in geophysical and astrophysical systems. Through the transport of mass, momentum and energy, they play a central role in shaping oceanic and atmospheric circulations (Andrews, Holton & Leovy 1987; Bühler 2014; Vallis 2017; Whalen *et al.* 2020; Le Bars 2023), and influence the internal dynamics of stars (Rogers *et al.* 2013). Recent studies have highlighted the significant impact of diapycnal mixing driven by internal gravity waves on a range of climate phenomena. However, accurately resolving the short vertical scales associated with these processes, particularly in climate simulations, remains challenging, underscoring the need for further theoretical modelling and systematic study of internal gravity wave dynamics (MacKinnon *et al.* 2017).

For strongly dispersive waves at sufficiently small amplitudes, weak wave turbulence theory provides a systematic framework for deriving a closed kinetic equation governing the slow evolution of the ensemble-averaged spectral energy density (Hasselmann 1966; Zakharov, L'vov & Falkovich 1992; Nazarenko 2011; Newell & Rumpf 2011; Galtier 2022). The first kinetic equation describing nonlinear interactions of three-dimensional internal waves in the presence of rotation was derived by Olbers (1976). Since then, the theory has been revisited using a variety of formalisms and assumptions (see, e.g. Pelinovsky & Raevsky 1977; Müller *et al.* 1986; Caillol & Zeitlin 2000; Lvov & Tabak 2001, 2004; Lvov, Polzin & Yokoyama 2012; Labarre *et al.* 2024*b*; Scott & Cambon 2024).

In the absence of rotation, and under the hydrostatic approximation – appropriate for motions with horizontal scales much larger than vertical scales – formal steady solutions of the kinetic equation have been obtained (Pelinovsky & Raevsky 1977; Caillol & Zeitlin 2000; Lvov & Tabak 2001). However, these solutions were later shown not to be physically realisable due to divergences in the collision integral (Caillol & Zeitlin 2000). Subsequent studies identified a unique bi-homogeneous steady spectrum yielding a convergent collision integral (Lvov *et al.* 2010; Dematteis & Lvov 2021); however, this three-dimensional prediction has not been observed in numerical simulations. More recently, within the hydrostatic limit, Lanchon & Cortet (2023) obtained steady solutions of a diffusion approximation to the kinetic equation that retains only induced-diffusion triadic interactions (McComas & Bretherton 1977).

It is important to note that the kinetic equation is not expected to hold in the vicinity of slow modes, where key assumptions underlying its derivation – such as Gaussian statistics and scale separation – break down (Galtier 2022). In particular, the accumulation of energy near zero vertical wavenumber leads to divergences in the collision integral unless a regularisation is introduced. A physical regularisation can be interpreted as considering the rotating–stratified Boussinesq equations in the limit of very small but finite rotation compared with stratification (Shavit, Bühler & Shatah 2026).

In two dimensions, using this approach, Shavit *et al.* (2025, 2026) found a steady solution of the full kinetic equation without invoking the hydrostatic approximation. The resulting turbulent energy spectrum is

$$e(\boldsymbol{k}) \propto k^{-3}\omega_{\boldsymbol{k}}^{-2}, \tag{1.1}$$

where $\boldsymbol{k} = (k_x, k_z)$ is the wave vector, $k = \sqrt{k_x^2 + k_z^2}$ its modulus, $\omega_{\boldsymbol{k}} = Nk_x/k$ the internal gravity wave frequency and N is the buoyancy (Brunt–Väisälä) frequency. Namely, $N = \sqrt{-(g/\rho_0)(\mathrm{d}\bar{\rho}/\mathrm{d}z)}$, where g is the acceleration due to gravity, ρ_0 is the reference density and $\bar{\rho}(z)$ the average density. Here, N quantifies the stratification of the fluid and usually depends on the elevation. Yet, it is common to assume that N is constant where the average density profile $\bar{\rho}(z)$ is nearly linear, as done by Shavit, Bühler & Shatah (2025). Expressed in frequency–vertical-wavenumber coordinates $(\omega_{\boldsymbol{k}}, k_z)$, the spectrum (1.1) coincides with the Garrett–Munk (GM) spectrum (Garrett & Munk 1979) in the limit of zero rotation and short vertical scales compared with the domain depth,

$$k^{-3}\omega_{\boldsymbol{k}}^{-2}\,\mathrm{d}k_x\,\mathrm{d}k_z = k_z^{-2}\omega_{\boldsymbol{k}}^{-2}\frac{1}{N}\,\mathrm{d}k_z\,\mathrm{d}\omega_{\boldsymbol{k}} \propto e_{\mathrm{GM}}. \tag{1.2}$$

Despite known deviations between measured oceanic spectra and the idealised GM form, the GM spectrum remains a useful reference for describing internal gravity wave statistics (Polzin *et al.* 2014; Dematteis *et al.* 2024).

Similar to other anisotropic dispersive waves in fluids, such as Rossby and inertial waves, internal gravity waves interact with slow modes, specifically domain, vortical and shear modes (Smith & Waleffe 2002; Laval, McWilliams & Dubrulle 2003; Brethouwer *et al.* 2007; Waite 2011; Remmel, Sukhatme & Smith 2014; Howland, Taylor & Caulfield 2020; Rodda *et al.* 2022). These slow modes present a significant challenge for the current weak wave turbulence description, which does not account for their evolution or interaction with dispersive waves. Their prominence in the energy spectrum complicates the observation of weak wave turbulence in internal gravity waves, both in direct numerical simulations (Remmel *et al.* 2014) and experiments (Lanchon *et al.* 2023). In particular, a well-observed feature of stratified turbulence is layering (see Caulfield 2021 and references therein), corresponding to an accumulation of energy in horizontal motions (shear and vortical modes) with the formation of well-mixed layers separated by sharp interfaces. If turbulence and stratification are strong enough, the layers' thickness is 'chosen' by the flow such that $L_z = U_{rms}/N$, where U_{rms} is the root mean square (r.m.s.) velocity of the large scale flow (Billant & Chomaz 2001; Brethouwer *et al.* 2007). This phenomenon looks like a self-organised criticality, where the flow organises itself such that the Richardson number is close to a critical value (Caulfield 2021), not far from the linear stability threshold (Howard 1961; Miles 1961).

Several mechanisms have been proposed to explain layer formation in strongly stratified turbulence. Early models based on the evolution of the mean density profile demonstrated that small perturbations to an initially linear stratification can grow when buoyancy fluxes decrease with increasing Richardson number (Phillips 1972). Reduced-order models incorporating turbulent kinetic energy and buoyancy evolution further clarified the conditions for layering (Balmforth *et al.* 1998; Taylor & Zhou 2017; Petropoulos, Mashayek & Caulfield 2023). From a dynamical standpoint, vortical modes are known to undergo zigzag instabilities that produce layers at the scale U/N (Billant & Chomaz 2000*a*,*b*). Notably, however, layering has also been observed in two-dimensional simulations (Smith 2001), in three-dimensional flows without vortical modes (Remmel *et al.* 2014), and even in systems where both vortical and shear modes are removed (Calpe Linares 2020; Labarre *et al.* 2024*a*). These observations suggest that layering can arise from wave dynamics alone, motivating the search for a wave-turbulence-based explanation.

In this work, we distinguish three regimes of two-dimensional stratified turbulence – discrete wave turbulence, weak wave turbulence and strong nonlinear interaction – within the parameter space defined by the Froude and Reynolds numbers. Using direct numerical simulation (DNS) of the Boussinesq equations with shear modes removed and employing hyperviscosity, we identify the conditions under which weak wave turbulence can be observed and provide the first DNS-based confirmation of the kinetic-theory prediction for internal gravity waves. Beyond the weakly nonlinear regime, we show that energy accumulation at slow frequencies leads to layer formation and derive scaling predictions for the resulting layer thickness and characteristic velocities in terms of the control parameters.

We remove shear modes to isolate dispersive wave interactions, reach statistically steady states efficiently and make direct comparisons with weak wave turbulence theory. The focus on two-dimensional flows is motivated by both practical and theoretical considerations. From a practical standpoint, two-dimensional (2-D) simulations are significantly less expensive than their three-dimensional (3-D) counterparts, allowing for extensive exploration of parameter space. From a theoretical perspective, the kinetic equation in 2-D (Shavit, Bühler & Shatah 2024) takes a simpler form due to the presence of an additional invariant and admits a theoretical prediction for the turbulent spectrum without invoking the hydrostatic approximation. While two-dimensional stratified flows do not capture interactions between gravity waves and vortical modes – present in three dimensions and crucial for vertical overturning and mixing – 2-D models nevertheless capture essential aspects of stratified dynamics and often serve as a first step towards understanding the full three-dimensional problem (Smith 2001; Boffetta *et al.* 2011; Fitzgerald & Farrell 2018; Calpe Linares 2020). Moreover, a two-dimensional description is directly relevant for laboratory experiments in long water tanks and for certain oceanic settings, such as internal tides radiated from isolated one-dimensional topographic features like the Hawaiian Ridge (Smith & Young 2003). In the weak wave turbulence regime, excluding low frequencies, our simulations show good agreement with recent theoretical predictions (Shavit *et al.* 2025). As layering develops and spectral peaks emerge at slow frequencies, our results highlight the limitations of the kinetic approach, while simultaneously providing a simple, physically grounded explanation for layer formation, including scaling laws for the characteristic velocity U and layer thickness L_z beyond the weakly nonlinear regime.

The remainder of the paper is organised as follows. In § 2, we introduce the governing equations and notation. In § 3, we identify the three turbulence regimes using wave-turbulence arguments. It emphasises that to observe the weak wave turbulence regime in a stratified fluid, a directed study must be done, which is crucial for experiments and future numerical investigations. The numerical set-up is described in § 4, and the results are analysed in § 5. We examine vorticity fields in § 5.1, one-dimensional spectra in § 5.2, and two-dimensional spectra and fluxes in § 5.3. A wave-turbulence-based interpretation of layer formation is presented in § 5.4, followed by a detailed comparison with theoretical predictions in § 5.5 and an analysis of Doppler shifts in § 5.6. Conclusions and perspectives are given in § 6.

2. Governing equations

2.1. *Dynamical equations*

Stratified flows can be described most simply using the Boussinesq equations, derived from the Euler equations by assuming a linear density profile in the vertical direction. For two-dimensional flows restricted to the vertical xz plane, the Boussinesq equations are

$$\nabla \cdot \boldsymbol{u} = 0, \tag{2.1}$$

$$\partial_t \boldsymbol{u} + \boldsymbol{u} \cdot \nabla \boldsymbol{u} = -\nabla p + b\boldsymbol{e}_z, \tag{2.2}$$

$$\partial_t b + \boldsymbol{u} \cdot \nabla b = -N^2 u_z, \tag{2.3}$$

where x and z are respectively the horizontal and vertical coordinates, $\boldsymbol{u} = (u_x, u_z)$ is the velocity field, p the kinematic pressure, b the buoyancy, and N is the buoyancy (or Brünt–Väisälä) frequency that we assume to be constant in this study. It is easy to check that (2.1)–(2.3) have two exact quadratic invariants: the total energy $E = (1/2)\int \mathrm{d}x\,\mathrm{d}z(\boldsymbol{u}\cdot\boldsymbol{u} + (b^2/N^2))$ and the correlation between vorticity, $\nabla^{\perp} \times \boldsymbol{u}$, and the buoyancy, called pseudomomentum $P = -\int \mathrm{d}x\,\mathrm{d}z(\nabla^{\perp} \times \boldsymbol{u})b$. We consider a periodic domain $\boldsymbol{x} = (x, z) \in [0, L]^2$ and expand the fields in terms of linear wave modes with wave vector $\boldsymbol{k} \in (2\pi\mathbb{Z}/L)^2$. We set $L = 2\pi$, so the x, z components of the wave vectors are integers. In polar coordinates, $\boldsymbol{k} = k(\cos\theta, \sin\theta)$, the dispersion relation is

$$\omega_{\boldsymbol{k}} = N\cos\theta. \tag{2.4}$$

Since the nonlinearity is quadratic, a resonant interaction of internal gravity waves is a triad $(\boldsymbol{k}, \boldsymbol{p}, \boldsymbol{q})$ satisfying

$$\omega_{\boldsymbol{k}} \pm \omega_{\boldsymbol{p}} \pm \omega_{\boldsymbol{q}} = 0. \tag{2.5}$$

For asymptotically weak nonlinearity, only exact resonances (2.5) occur. Yet, for realistic cases with finite nonlinearities, we rather observe pseudo-resonances such that

$$0 \leqslant \left|\omega_{\boldsymbol{k}} \pm \omega_{\boldsymbol{p}} \pm \omega_{\boldsymbol{q}}\right| \lesssim \omega_{nl}, \tag{2.6}$$

where ω_{nl} is due to nonlinear interactions and is called the nonlinear frequency broadening (Bourouiba 2008; L'vov & Nazarenko 2010; Buckmaster *et al.* 2021). Here, ω_{nl} corresponds to an energy transfer rate due to nonlinear interactions. It depends on the triads and the wave energy spectrum.

2.2. *Forcing, dissipation and energy transfers*

We add forcing and dissipation to the dynamical equations to study the statistics of stationary turbulent states. Specifically, we force the system (2.1)–(2.3) at small wave vectors and add significant dissipation at large wave vectors. Rewriting the dynamical equations in terms of the stream function ψ, $(u_x, u_z) = (-\partial_z\psi, \partial_x\psi)$, with forcing and dissipation yields

$$\partial_t\Delta\psi + \{\psi, \Delta\psi\} = \partial_x b + \Delta f_\psi + (-1)^{n-1}\nu_n\Delta^n(\Delta\psi), \tag{2.7}$$

$$\partial_t b + \{\psi, b\} = -N^2\partial_x\psi + f_b + (-1)^{n-1}\kappa_n\Delta^n b. \tag{2.8}$$

Here, $-\Delta\psi$ is the vorticity, $\{G, F\} = \partial_x G\partial_z F - \partial_z G\partial_x F$. Additionally, f_ψ and f_b are respectively the stream function and buoyancy forcing. Furthermore, ν_n is the hyperviscosity and κ_n the hyperdiffusivity. In this study, we set $\kappa_n = \nu_n$. One recovers the standard Boussinesq equations for $n = 1$. Using hyperviscosity and hyperdiffusion is a standard method to enlarge the inertial range at a given resolution (Brethouwer *et al.* 2007).

In Fourier space, (2.7)–(2.8) read

$$\partial_t\hat{\psi}_{\boldsymbol{k}} - \frac{1}{k^2}\widehat{\{\psi, \Delta\psi\}}_{\boldsymbol{k}} = i\frac{k_x}{k^2}\hat{b}_{\boldsymbol{k}} + \hat{f}_{\psi,\boldsymbol{k}} + (-1)^{n-1}\nu_n(-k^2)^n\hat{\psi}_{\boldsymbol{k}}, \tag{2.9}$$

$$\partial_t\hat{b}_{\boldsymbol{k}} + \widehat{\{\psi, b\}}_{\boldsymbol{k}} = ik_xN^2\hat{\psi}_{\boldsymbol{k}} + \hat{f}_{b,\boldsymbol{k}} + (-1)^{n-1}\kappa_n(-k^2)^n\hat{b}_{\boldsymbol{k}}, \tag{2.10}$$

where $\hat{(\cdot)}_{\boldsymbol{k}}$ denotes the Fourier transform. It follows that the equations for the kinetic energy spectrum $e_{kin}(\boldsymbol{k}, t) = \left|\hat{\boldsymbol{u}}_{\boldsymbol{k}}\right|^2/2 = k^2|\hat{\psi}_{\boldsymbol{k}}|^2/2$ and the potential energy spectrum $e_{pot}(\boldsymbol{k}, t) = |\hat{b}_{\boldsymbol{k}}|^2/(2N^2)$ read

$$\partial_t e_{kin}(\boldsymbol{k}, t) = -\mathcal{T}_{kin}(\boldsymbol{k}, t) - \mathcal{C}(\boldsymbol{k}, t) + \mathcal{F}_{kin}(\boldsymbol{k}, t) - \mathcal{D}_{kin}(\boldsymbol{k}, t), \tag{2.11}$$

$$\partial_t e_{pot}(\boldsymbol{k}, t) = -\mathcal{T}_{pot}(\boldsymbol{k}, t) + \mathcal{C}(\boldsymbol{k}, t) + \mathcal{F}_{pot}(\boldsymbol{k}, t) - \mathcal{D}_{pot}(\boldsymbol{k}, t). \tag{2.12}$$

The kinetic and potential energy transfers are defined by

$$\mathcal{T}_{kin}(\boldsymbol{k}, t) = -\mathrm{Re}\left(\hat{\psi}^*_{\boldsymbol{k}}\widehat{\{\psi, \Delta\psi\}}_{\boldsymbol{k}}\right) \quad \text{and} \quad \mathcal{T}_{pot}(\boldsymbol{k}, t) = \frac{1}{N^2}\mathrm{Re}\left(\hat{b}^*_{\boldsymbol{k}}\widehat{\{\psi, b\}}_{\boldsymbol{k}}\right), \tag{2.13}$$

respectively, where $(\cdot)^*$ is the complex conjugate, $\mathrm{Re}(\cdot)$ is the real part and $\mathrm{Im}(\cdot)$ is the imaginary part. Physically, $\mathcal{T}_{kin}$ and $\mathcal{T}_{pot}$ represent the kinetic and potential energy transfers from mode $\boldsymbol{k}$ through nonlinear interactions per unit time. The kinetic and potential energy dissipation rates are

$$\mathcal{D}_{kin}(\boldsymbol{k},t) = 2\nu_n k^{2n} e_{kin}(\boldsymbol{k},t) \quad \text{and} \quad \mathcal{D}_{pot}(\boldsymbol{k},t) = 2\kappa_n k^{2n} e_{pot}(\boldsymbol{k},t). \tag{2.14}$$

The kinetic and potential energy injection rates are

$$\mathcal{F}_{kin}(\boldsymbol{k},t) = \mathrm{Re}\left(k^2 \hat{f}_{\psi,\boldsymbol{k}} \hat{\psi}^*_{\boldsymbol{k}}\right) \quad \text{and} \quad \mathcal{F}_{pot}(\boldsymbol{k},t) = \frac{1}{N^2}\mathrm{Re}\left(\hat{f}_{b,\boldsymbol{k}} \hat{b}^*_{\boldsymbol{k}}\right). \tag{2.15}$$

Finally, the conversion of kinetic energy into potential energy is

$$\mathcal{C}(\boldsymbol{k},t) = \mathrm{Im}\left(k_x \hat{b}_{\boldsymbol{k}} \hat{\psi}^*_{\boldsymbol{k}}\right). \tag{2.16}$$

We denote the total energy spectrum $e = e_{kin} + e_{pot}$, the total energy transfer $\mathcal{T} = \mathcal{T}_{kin} + \mathcal{T}_{pot}$, the total energy dissipation rate $\mathcal{D} = \mathcal{D}_{kin} + \mathcal{D}_{pot}$ and the total energy injection rate $\mathcal{F} = \mathcal{F}_{kin} + \mathcal{F}_{pot}$. We note the one-dimensional (1-D) kinetic energy transfers as

$$\Pi_{kin}(k,t) = \sum_{\boldsymbol{k}', |\boldsymbol{k}'| \leqslant k} \mathcal{T}_{kin}(\boldsymbol{k}',t), \tag{2.17}$$

$$\Pi_{kin}(\omega_{\boldsymbol{k}},t) = \sum_{\boldsymbol{k}', |\omega_{\boldsymbol{k}'}| \leqslant \omega_{\boldsymbol{k}}} \mathcal{T}_{kin}(\boldsymbol{k}',t). \tag{2.18}$$

They represent respectively the kinetic energy transfer to modes with wave vector modulus larger than k and the kinetic energy transfer to modes with wave frequency larger than $\omega_{\boldsymbol{k}}$. We use similar definitions for the 1-D potential and total energy transfers. We also introduce the 1-D conversion rates

$$C(k,t) = \sum_{\boldsymbol{k}', k-1 \leqslant |\boldsymbol{k}'| < k} \mathcal{C}(\boldsymbol{k}',t), \tag{2.19}$$

$$C(\omega_{\boldsymbol{k}},t) = \sum_{\boldsymbol{k}', \omega_{\boldsymbol{k}} - \delta\omega_{\boldsymbol{k}} \leqslant |\omega_{\boldsymbol{k}'}| < \omega_{\boldsymbol{k}}} \mathcal{C}(\boldsymbol{k}',t), \tag{2.20}$$

which correspond to the rate of conversion from kinetic energy to potential energy for modes with wave vectors $\simeq k$ and wave frequencies $\simeq \omega_{\boldsymbol{k}}$, respectively. We use the frequency increment $\delta\omega_{\boldsymbol{k}} = N/64$ to compute the energy transfers numerically.

3. Parametric regimes

The standard dimensionless parameters for a stratified fluid are the Froude number, which quantifies stratification strength, and the (hyper-viscous) Reynolds number, representing the balance between dissipation and nonlinear interaction:

$$Fr \equiv \frac{Uk_f}{N} \quad \text{and} \quad Re_n \equiv \frac{U}{\nu_n k_f^{2n-1}}, \tag{3.1}$$

where U is a typical velocity. In this study, we choose U as the typical velocity fluctuation due to the forcing mechanism. It should depend on the forcing characteristics only, as long as the forced wave vectors are not in the dissipative range. Then, from dimensional analysis, we fix $U = (\varepsilon/k_f)^{1/3}$ with k_f the typical wavevector modulus of forced waves and ε the energy injection rate. The Froude number is then the ratio estimating the destabilising effect of the forcing on the flow compared with the stabilising effect of the buoyancy force. Note that U should not depend on the regime (strongly stratified or weakly stratified turbulence) and that U differs from the root mean square velocity U_{rms} used in many other studies (Billant & Chomaz 2001; Brethouwer *et al.* 2007).

One characterises stratified turbulence by several length scales. First, we define the buoyancy wavevector

$$k_b \equiv \frac{N}{U} = k_f Fr^{-1}. \tag{3.2}$$

For scales larger than $2\pi/k_b$, linear terms dominate over nonlinear ones in the dynamical equations (2.1)–(2.3). Second, we define the Ozmidov wavevector

$$k_O \equiv \sqrt{\frac{N^3}{\varepsilon}} = k_f Fr^{-3/2}. \tag{3.3}$$

The Ozmidov scale $\propto 1/k_O$ is generally interpreted as, for a given flow, the largest horizontal scale that can overturn or, similarly, the scale at which buoyancy forces and inertial forces are comparable (Riley & Lindborg 2008). Third, the Kolmogorov wave vector

$$k_\eta \equiv \left(\frac{\varepsilon}{\nu_n^3}\right)^{1/(6n-2)} = k_f Re_n^{3/(6n-2)} \tag{3.4}$$

is representative of the scale under which energy dissipation is important, marking the transition between the inertial and dissipative ranges.

We now identify three regimes: discrete wave turbulence, weak wave turbulence and strong turbulence. To observe weak wave turbulence:

(i) wave amplitudes must be small to ensure weak nonlinear interactions;
(ii) the number of pseudo-resonances – meaning triadic interactions satisfying (2.6) – needs to be large to ensure pseudo-continuous energy exchanges between waves (Bourouiba 2008; L'vov & Nazarenko 2010; Buckmaster *et al.* 2021).

Here, we will use a condition more restrictive than condition (i). Namely, that the flow must be composed of weakly nonlinear waves only, so it is not perturbed by structures not considered in the theory, such as small-scale eddies. This condition is achieved if dissipation occurs at scales larger than the buoyancy scale, implying

$$k_\eta \lesssim k_b \;\Rightarrow\; Re_n \lesssim Fr^{(2-6n)/3}. \tag{3.5}$$

Therefore, for weak wave turbulence to occur, the Reynolds number cannot be arbitrarily large, as shown in prior studies on internal wave turbulence (Le Reun *et al.* 2017, 2018; Brunet, Gallet & Cortet 2020). When condition (3.5) is not met, wave breaking is likely, leading to strongly nonlinear stratified turbulence. To ensure condition (ii), the nonlinear frequency broadening ω_{nl} (2.6) must exceed the wave frequency gap in discrete Fourier space $|\boldsymbol{\nabla}_{\boldsymbol{k}}\omega_{\boldsymbol{k}} \boldsymbol{\cdot} \mathrm{d}\boldsymbol{k}|$, with $\mathrm{d}\boldsymbol{k} = (2\pi s_x/L, 2\pi s_z/L)$ being the wavevector gap between adjacent modes (L'vov & Nazarenko 2010). For a given $\boldsymbol{k}$, we assume that the nonlinear frequency broadening depends only on the energy injection rate and $k = |\boldsymbol{k}|$ such that $\omega_{nl} = (\varepsilon k^2)^{1/3}$. It is a strong simplification. Obtaining a better estimate is complicated since ω_{nl} depends on the details of the triadic interactions and on the energy spectrum. In addition, this estimate gives realistic predictions. Then, to satisfy condition (ii), we require that

$$|\boldsymbol{\nabla}_{\boldsymbol{k}}\omega_{\boldsymbol{k}} \boldsymbol{\cdot} \mathrm{d}\boldsymbol{k}| \lesssim \omega_{nl} \tag{3.6}$$

$$\Rightarrow \quad \frac{2\pi}{L}\left| s_x \frac{\partial \omega_{\boldsymbol{k}}}{\partial k_x} + s_z \frac{\partial \omega_{\boldsymbol{k}}}{\partial k_z}\right| \lesssim \left(\varepsilon k^2\right)^{1/3} \tag{3.7}$$

$$\Rightarrow \quad \frac{2\pi N}{Lk} |\sin\theta|\, |s_x \sin\theta - s_z \cos\theta| \lesssim \left(U^3 k_f k^2\right)^{1/3}. \tag{3.8}$$

The prefactor $|\sin\theta|$ implies that the inequality is more likely to be violated at $\theta \simeq \pm\pi/2$, i.e. for small wave frequencies $\omega_{\boldsymbol{k}} = N\cos\theta$. Ensuring this condition across all angles θ and $s_x, s_z = 0, \pm 1$ reduces to

$$kL \gtrsim (2\pi)^{3/5} (Lk_f)^{2/5} Fr^{-3/5}. \tag{3.9}$$

To simplify, we consider only large-scale forcing for which $Lk_f \sim 1$. Then, the previous condition reads

$$k \gtrsim k_c \equiv c k_f Fr^{-3/5}, \tag{3.10}$$

where c is an empirical numerical factor that we cannot determine with our reasoning based on dimensional analysis. The factor c can depend, among other things, on the forcing mechanism and the aspect ratio of the fluid domain. In the present study, we fix this factor to a constant value $c = 0.31$ for comparing our predictions to simulations, even when they employ different forcing mechanisms (Appendix). We expect the interaction to be concentrated on discrete sets of modes with slow wave frequencies and wavevectors modulus $k \lesssim k_c$, leading to discrete wave turbulence (L'vov & Nazarenko 2010). For observing a weak wave turbulence range in the energy spectra, one needs to satisfy

$$k_\eta \gg k_c \;\Rightarrow\; Re_n \gg c^{(6n-2)/3} Fr^{(2-6n)/5}. \tag{3.11}$$

Otherwise, the fluid is expected to be in a discrete wave turbulence regime. This observation is crucial for laboratory experiments interested in the weak wave turbulence regime. As our numerical results show in the next section, k_c plays an important role in strongly stratified turbulence simulations. Analogous conditions to (3.5) and (3.11) are also necessary to make comparisons with weak wave turbulence theory for quantum fluids (Zhu *et al.* 2022), surface waves (Falcon & Mordant 2022) and other systems.

In the weak wave turbulence regime, one has a separation between the linear time and the kinetic time. The linear time $\sim 1/\omega_{\boldsymbol{k}}$ corresponds to the wave oscillations, while the kinetic time $Fr^{-2}/\omega_{\boldsymbol{k}}$ (Nazarenko 2011) corresponds to the typical time scale of the evolution of the energy spectrum due to wave–wave interactions. The flow reaches a steady state only after several kinetic times. Consequently, the smaller the Froude number, the better the time scale separation, but the longer the numerical simulation/experiment to reach a steady state.

For our simulations, we found it convenient to introduce another length-scale, characterised by the wavevector

$$k_d \equiv \left(\frac{U}{\nu_n}\right)^{1/(2n-1)} = k_f Re_n^{1/(2n-1)} \tag{3.12}$$

to set the hyper-viscosity for having well-resolved simulations. Namely, fixing a constant ratio k_{max}/k_d allowed us to have well-resolved simulations for all Fr, Re_n. In contrast, we have observed blow-ups for some simulations at large Re_n when we tried to fix a constant k_{max}/k_η. Then, working with k_d allowed us to have a unique criterion for fixing viscosity for all simulations.

When using hyperviscosity, it is more natural to use length-scales' ratios (instead of Re_n) to discuss transitions between regimes Brethouwer *et al.* (2007), Waite (2011). We introduced seven typical wave vectors: $1/L$, k_f, k_c, k_b, k_O, k_η and k_d, so we can use six ratios of these wavevectors to distinguish between flow regimes. We focus on large-scale forcing $Lk_f \sim 1$, in turbulent regimes $k_\eta/k_f \gg 1$. Also, $k_d/k_\eta = Re_n^{1/(2n-1)(6n-2)} \sim 1$ in the investigated parameters range. To discuss the transitions to weak wave turbulence regime, we use the two ratios

$$\frac{k_f}{k_b} = Fr \quad \text{and} \quad \frac{k_b}{k_\eta} = Fr^{-1} Re_n^{-3/(6n-2)}. \tag{3.13}$$

The definitions of k_O (3.3) and k_c (3.10) fix k_O and k_c in terms of Fr and k_b/k_η. The conditions for a weak wave turbulence regime then read

$$\frac{k_f}{k_b} = Fr \ll 1, \quad \frac{k_b}{k_\eta} \gtrsim 1 \quad \text{and} \quad \frac{k_\eta}{k_c} \gg 1 \;\Rightarrow\; \frac{k_b}{k_\eta} \ll \frac{1}{c} Fr^{-2/5}. \tag{3.14}$$

We will talk about strongly nonlinear regimes for $k_b/k_\eta \lesssim 1$ and the discrete wave turbulence regime for $k_\eta/k_c \lesssim 1$. We will also distinguish between weakly stratified regimes, for which $k_c \leqslant k_f$, and the strongly stratified regimes, for which $k_c \geqslant k_f$. Using (3.10), these regimes are delimited by a critical Froude number $Fr_c = c^{5/3} = 0.14$. In the weakly stratified regime, k_c lies in the forcing range. Then, the random forcing perturbs modes at $k = k_c$ such as horizontal flows, which may inhibit their evolution. In contrast, in the strongly stratified regime, k_c lies outside the forcing range. Then, modes at $k = k_c$ are freer to develop when compared with the weakly stratified regime.

Finally, our analysis assumes that the typical velocity fluctuation due to the forcing U is determined solely by the input parameters ε and k_f. The observed deviations of the measured r.m.s. velocity in our simulations are discussed in § 5. In this section, we also connect our definitions to standard definitions used in studies of stratified flows, using an approximation of the r.m.s. velocity based on the discrete wave regime.

4. Simulations

4.1. *Numerical methods*

We perform forced-dissipated DNS of (2.7)–(2.8) in a square periodic domain of size $L = 2\pi$ using a pseudo-spectral method with a standard 2/3 rule for dealising. We force the flow with two independent white noise terms for the stream function and the buoyancy for modes such that the forcing amplitudes are non-zero on a bounded ring $|\boldsymbol{k}| \in [k_{f,min}, k_{f,max}]$ and $k_x, k_y \neq 0$. Without considering other terms but forcing, the dynamical equation for the stream function of forced modes reads

$$\mathrm{d}\hat{\psi}_{\boldsymbol{k}} = \hat{f}_{\psi,\boldsymbol{k}}\, \mathrm{d}t = \sqrt{\varepsilon\, \mathrm{d}t}\, \frac{X_{\boldsymbol{k}} + X^*_{-\boldsymbol{k}}}{\sqrt{\sum_{\boldsymbol{k}} \left| X_{\boldsymbol{k}} + X^*_{-\boldsymbol{k}} \right|^2 k^2}}, \tag{4.1}$$

where $X_{\boldsymbol{k}}$ are complex numbers whose real and imaginary parts are normal random variables. It ensures a real forcing in physical space with a constant kinetic energy injection rate $\sum_{\boldsymbol{k}} |\hat{f}_{\psi,\boldsymbol{k}}\, \mathrm{d}t\, k|^2/(2\, \mathrm{d}t) = \varepsilon/2$. The equivalent of (4.1) for the buoyancy is $\mathrm{d}\hat{b}_{\boldsymbol{k}} = \hat{f}_{b,\boldsymbol{k}}\, \mathrm{d}t$, where $\hat{f}_{b,\boldsymbol{k}}$ is obtained in the same way as $\hat{f}_{\psi,\boldsymbol{k}}$, up to a prefactor $-Nk$, and using an independent stochastic process. Doing so, the potential energy injection is equal to $\sum_{\boldsymbol{k}} |(\hat{f}_{b,\boldsymbol{k}}/N)\, \mathrm{d}t|^2/(2\mathrm{d}t) = \varepsilon/2$. The independence of f_ψ and f_b ensures that the pseudomomentum is zero on average, $\langle P \rangle = 0$. The parameters that quantify the forcing are therefore the average energy injection rate ε and the wavevector modulus at the middle of the forcing ring $k_f = (k_{f,max} + k_{f,min})/2$. For the white noise forcing (4.1), we set

$$[k_{f,min}, k_{f,max}] = [0.9; 5.1] \;\Rightarrow\; k_f = \frac{k_{f,min} + k_{f,max}}{2} = 3 \quad \text{and} \quad \varepsilon = 10^{-3}. \tag{4.2}$$

M	**N**
128	1, 2, 4, 8, 16, 32*
256	1, 2, 4, 8, 16, 32*
512	1, 2, 4, 8, 16
1024	1, 2, 4, 8, 16*
2048	1, 2, 4, 8*

Table 1. List of our simulations with relevant control parameters. We set $L = 2\pi$, $n = 4$, $\varepsilon = 10^{-3}$, $k_f = 3$ and $k_{max}/k_d = 1.5$. Therefore, the dimensionless parameters (3.1) are then given by $Fr = 0.1 \times 3^{2/3}/N$ and $Re_n = (2M/27)^7$. Except for simulations with an $*$, we ran simulations with either buoyancy forcing or velocity forcing, which we present in the Appendix.

For time advancement, we employ the fractional-step splitting method (McLachlan & Quispel 2002). Namely, we apply the linear operator for a time increment $\mathrm{d}t/2$, compute the contribution of the nonlinear term using the Runge–Kutta 2 method and apply the linear operator for $\mathrm{d}t/2$. This method has the advantage of treating the linear terms explicitly and achieving second-order precision. We denote by M the number of grid points in each direction. The hyperviscosity order is set to $n = 4$ and the hyperviscosity ν_n is fixed such that the ratio between the maximal wavevector modulus $k_{max} = M/3$ and the viscous wavevector k_d (3.12) is $k_{max}/k_d = 1.5$. The time step $\mathrm{d}t$ is the minimum between $10^{-2}/N$ and the time step given by a Courant–Friedrichs–Lewy (CFL) number 0.65. These choices allow us to obtain well-resolved simulations for the investigated range of parameters.

We remove shear modes, i.e. modes with $k_x = 0$, by forbidding energy transfers to these modes. We prevent energy from going to the shear modes by setting the amplitude of the energy transfers to these modes to zero at each time step of the simulation. Hence, there is no flux of energy towards the shear modes (Calpe Linares 2020; Labarre *et al.* 2024*a*).

4.2. *Setting up the data set*

To construct our dataset, we first run simulations at a small resolution $M = 128$. We start simulations with $M \geqslant 256$ from the end of the simulation at the same N with lower resolution $M/2$ and decrease the viscosity as we increase the resolution. It allows us to save computational time and reach statistically steady states faster. The simulation time of the small resolution simulations, i.e. $M = 128$, is $\propto 400N$. For the other simulations, i.e. $M \geqslant 256$, the simulation time is $\propto 200N$. Then, our runs are much longer than the kinetic time, which is necessary to reach a statistically steady state of weak internal gravity wave turbulence. We give the list of the simulations, with the values of the relevant parameters, in table 1.

In figure 1, we show the energy dissipation rate signals for our simulations. We observe that we reach a statistically steady state, characterised by constant energy dissipation rates $\mathcal{D}_{kin}$ and $\mathcal{D}_{pot}$, with total energy dissipation equal to energy injection, i.e. $\mathcal{D} = \mathcal{D}_{kin} + \mathcal{D}_{pot} = \varepsilon$. The steady state is reached in less than $\propto 100N$ time units for all simulations. For the largest Fr, shown in panel (*a*), the resolution is doubled four times (at $t/N = 400$, 600, 800 and 1000), allowing the study of five different values of k_b/k_η. As we increase k_η by increasing resolution, the potential energy dissipation gets bigger while the kinetic energy dissipation rate gets smaller. For intermediate Fr, shown in panel (*b*), we observe the same behaviour. Yet, $\mathcal{D}_{pot} \sim \mathcal{D}_{kin}$ even for the largest k_η investigated. For the lowest Fr, shown in panel (*c*), we doubled the resolution only once due to the prohibitive computation time. In these simulations, $\mathcal{D}_{pot} \simeq \mathcal{D}_{kin}$, which is because the flow is composed only of weakly nonlinear waves. As we decrease Fr, the amplitude of dissipation fluctuations increases.

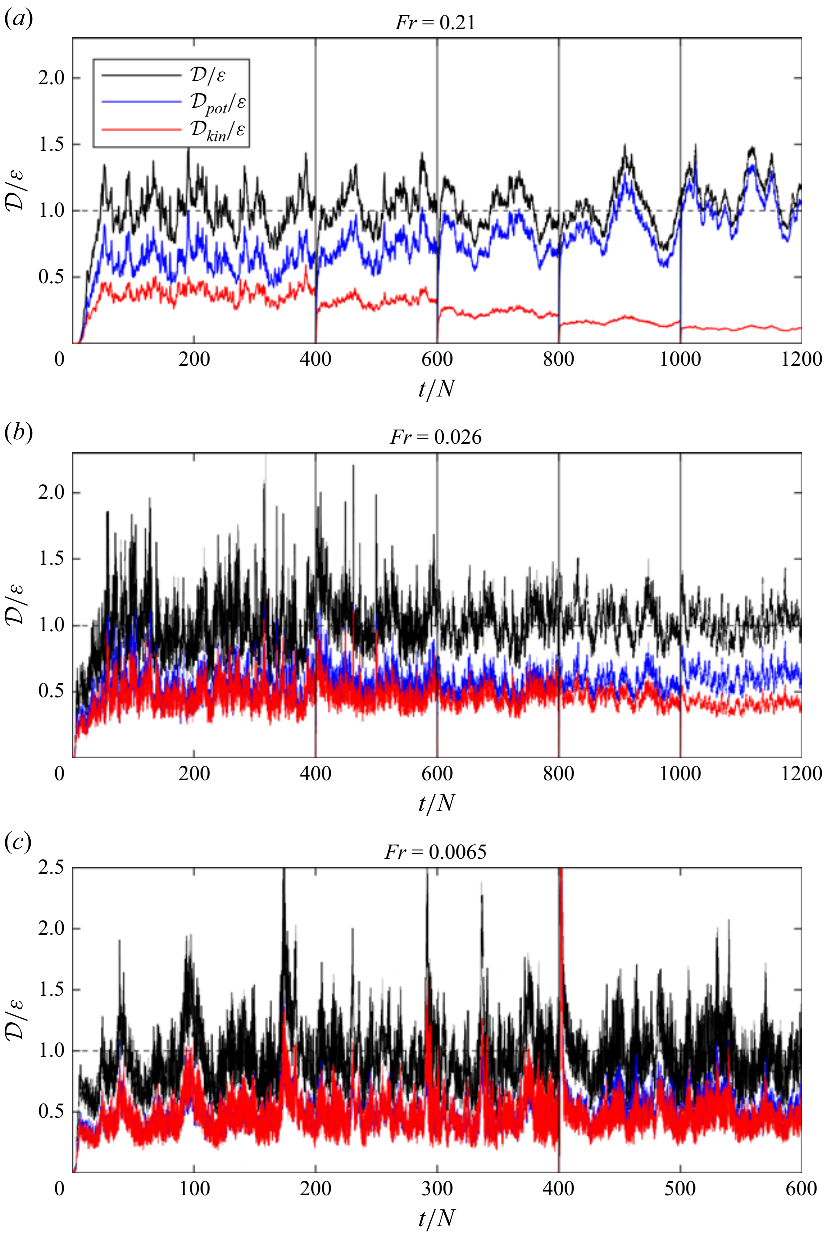

Figure 1. Normalised energy dissipation rate signals for simulations with three different Froude numbers. The black vertical lines indicate times at which we double resolution, so we increase k_η.

5. Study of the flow regimes

We present our simulations on the parametric $(k_f/k_b = Fr, k_b/k_\eta)$ plane and the transition lines for the expected regimes in figure 2(*a*). In figure 2(*b*), we plot the ratio between the r.m.s velocity $U_{rms} = \sqrt{2E_{kin}}$ and the typical velocity fluctuation due to the forcing $U = (\varepsilon/k_f)^{1/3}$, where E_{kin} is the total kinetic energy. This ratio decreases like $Fr^{-2/5}$ and is weakly dependent on k_b/k_η.

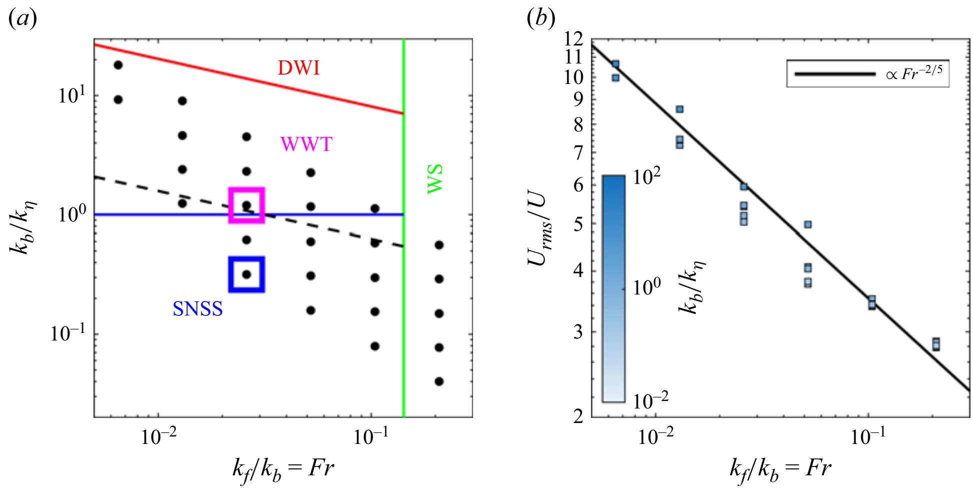

Figure 2. (*a*) Simulations on the parametric plane ($k_f/k_b = Fr$, k_b/k_η). The green line represents $k_c = k_f$, which separates the weakly stratified (WS) regimes from the strongly stratified regimes. The blue line represents $k_b = k_\eta$ (3.5), which separates the weak wave turbulence (WWT) from the strong nonlinear – strongly stratified regime (SNSS). The red line indicates $k_c = k_\eta$ (3.11), distinguishing the weak wave turbulence from the discrete wave interaction (DWI) regimes. The dashed line corresponds to the transition (5.13), with $\alpha = 4$. The blue box highlights the simulation whose spectra are shown in figure 5. The magenta box indicates the simulation whose spectra are shown in figure 7. (*b*) Ratio between the r.m.s. velocity U_{rms} and the typical velocity fluctuation due to the forcing $U = (\varepsilon/k_f)^{1/3}$ as a function of Fr for all simulations with varying k_b/k_η. The solid line corresponds to the theoretical scaling (5.6).

5.1. *Vorticity structure across regimes*

In figure 3, we present the vorticity field in the statistically steady state for four simulations. When stratification is weak (Fr is large) and small k_b/k_η, we observe 2-D vortices without layering (figure 3*a*). As k_b/k_η decreases, smaller vortices appear (figure 3*b*), as expected due to the extension of the inertial range. With stronger stratification (smaller Fr), we observe layering in the vorticity field (figure 3*c*). This phenomenon has been reported previously in simulations without shear modes (Calpe Linares 2020). Notably, the layers' thickness remains unchanged after further decreases in k_b/k_η; while the vortices become smaller (figure 3*d*).

5.2. *Energy spectra across regimes*

In figure 4, we present the compensated 1-D spectra

$$e(k,t) = \sum_{\boldsymbol{k}', k-1 \leqslant k' < k} e(\boldsymbol{k}, t), \tag{5.1}$$

averaged over time in the steady state, for four simulations across various regimes: (a) strong nonlinear–weakly stratified regime (WS); (b) strong nonlinear–strongly stratified regime (SNSS); (c) weak wave turbulence (WWT); and (d) discrete wave interaction (DWI).

When the stratification is weak and the nonlinearity is strong, region (a), the potential energy spectrum differs from the kinetic energy spectrum, particularly for $k > k_O$. The spectra are continuous, except at the end of the forcing range. In this case, we observe a good agreement with the Bolgiano–Obukhov scalings in the range $k \in [k_O : k_\eta]$ (see § 4.4.1 of Alexakis & Biferale 2018 and references therein). Namely, we observe that the

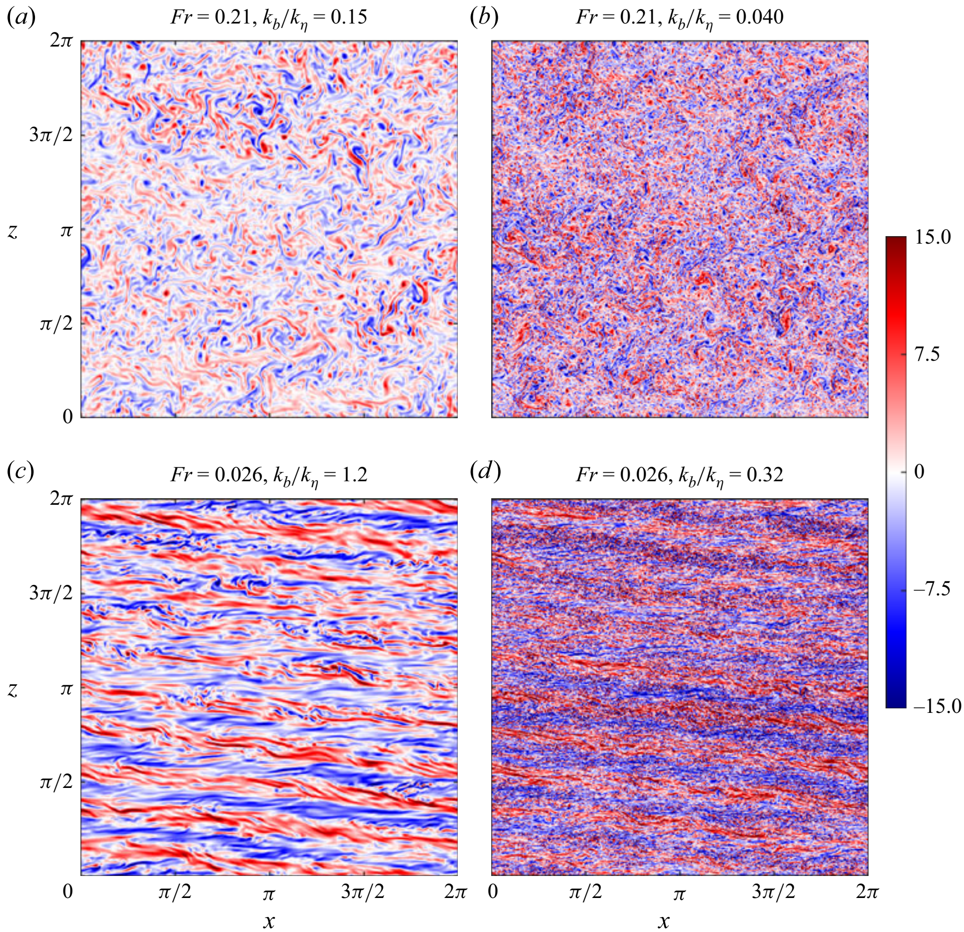

Figure 3. Vorticity field in the statistically steady state for simulations with different Fr and k_b/k_η.

kinetic energy spectrum is roughly $\propto \varepsilon^{2/5} N^{4/5} k^{-11/5}$ and the potential energy spectrum is close to $\propto \varepsilon^{4/5} N^{-2/5} k^{-7/5}$. As stratification increases, region (b), both k_b and k_O become larger, leading to closer alignment between the kinetic and potential energy spectra across a broader range. In this simulation, nearly all energetic scales are influenced by stratification, as $k_O \simeq k_\eta$. In the weak wave turbulence regime (c), characterised by intermediate stratification and nonlinearity, we satisfy condition (3.5) so all energetic scales are expected to interact through weak nonlinearity. The potential and kinetic energy spectra are nearly equal across all scales, which is typical for internal gravity waves. Yet, the energy spectrum peaks around $k = 13$, with only the range $k \gtrsim 13$ appearing continuous. The peak, which corresponds to the layering, also perturbs the scaling for large wavevectors $k \geqslant 13$ and we do not observe the theoretical scaling in this simulation. For the simulation in panel (*d*), the stratification is the highest and nonlinearity is the weakest such that condition (3.11) is almost violated. In this regime, energetic scales interact predominantly through a discrete set of interactions, as evidenced by the numerous discrete peaks in the spectrum. It confirms that the simulation corresponds to the discrete wave interaction regime.

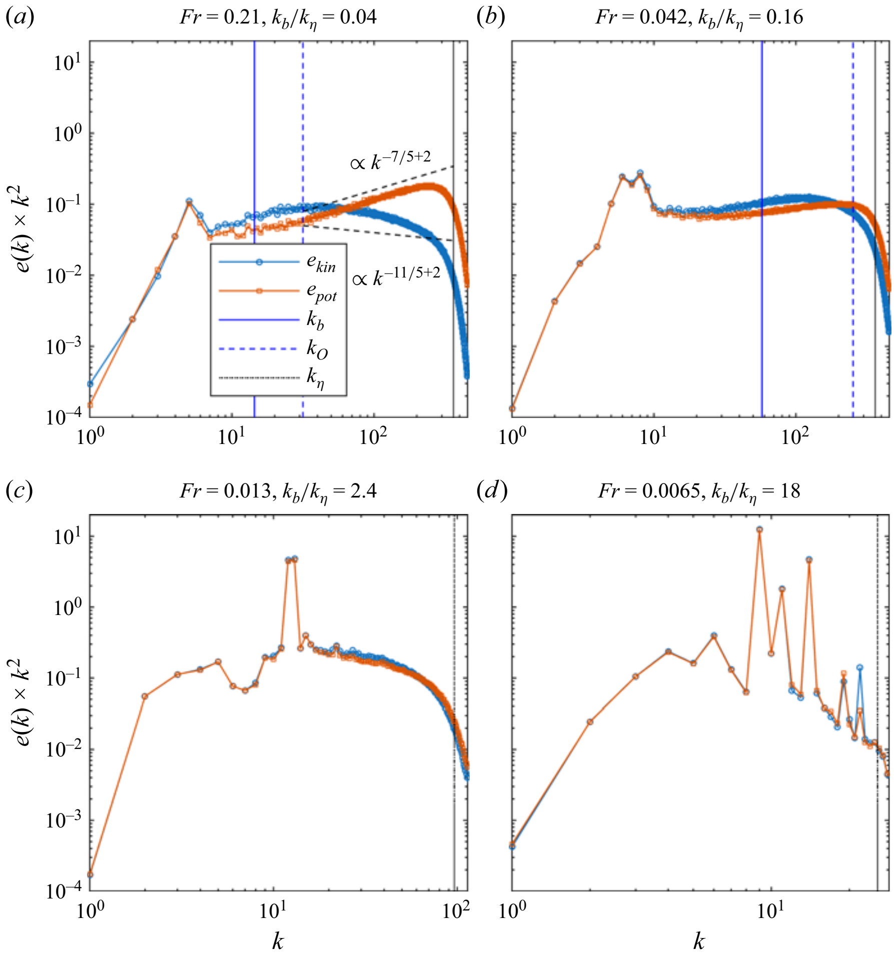

Figure 4. 1-D kinetic and potential energy spectra for four simulations, compensated by k^2. Vertical lines correspond to buoyancy, Ozmidov and Kolmogorov wave vectors k_b, k_O and k_η. For each panel, we show only the range $k \in [1 : k_d]$, which contains almost all the energy. In panel (*a*), we show the Bolgiano–Obukhov scalings, $e_{kin} \propto k^{-11/5}$ and $e_{pot} \propto k^{7/5}$, as dashed lines.

5.3. *Strong nonlinearity regime*

To compare to the analytical prediction (1.1), we introduce the $(k, |\omega_{\boldsymbol{k}}/N|)$ energy spectra, defined as

$$e\,(k, |\omega_{\boldsymbol{k}}/N|, t) = \sum_{s_x, s_z = \pm 1} e(k_x = s_x k |\omega_{\boldsymbol{k}}/N|, k_z = s_z k \sqrt{1 - (\omega_{\boldsymbol{k}}/N)^2}, t), \qquad (5.2)$$

where we use bilinear interpolations of the (k_x, k_z) energy spectrum to estimate $e(k_x = s_x k|\omega_{\boldsymbol{k}}/N|, k_z = s_z k\sqrt{1-(\omega_{\boldsymbol{k}}/N)^2})$ for a given $(k, |\omega_{\boldsymbol{k}}/N|)$.

In figure 5(*a*,*b*), we show slices of the $(k, |\omega_{\boldsymbol{k}}/N|)$ energy spectra, averaged over time in the steady state, at various frequencies as a function of the wavevector amplitude k, compensated by the weak wave turbulence prediction (1.1), for a simulation in the strong nonlinearity regime. We see in panel (*a*) that the kinetic energy spectrum is shallower than k^{-3}, and has a bump at $k \simeq k_b$ and high $\omega_{\boldsymbol{k}}$, as observed in earlier studies (see e.g. Waite 2011; Augier, Billant & Chomaz 2015). For slow frequencies $\omega_{\boldsymbol{k}}/N = 0.1$, we observe a

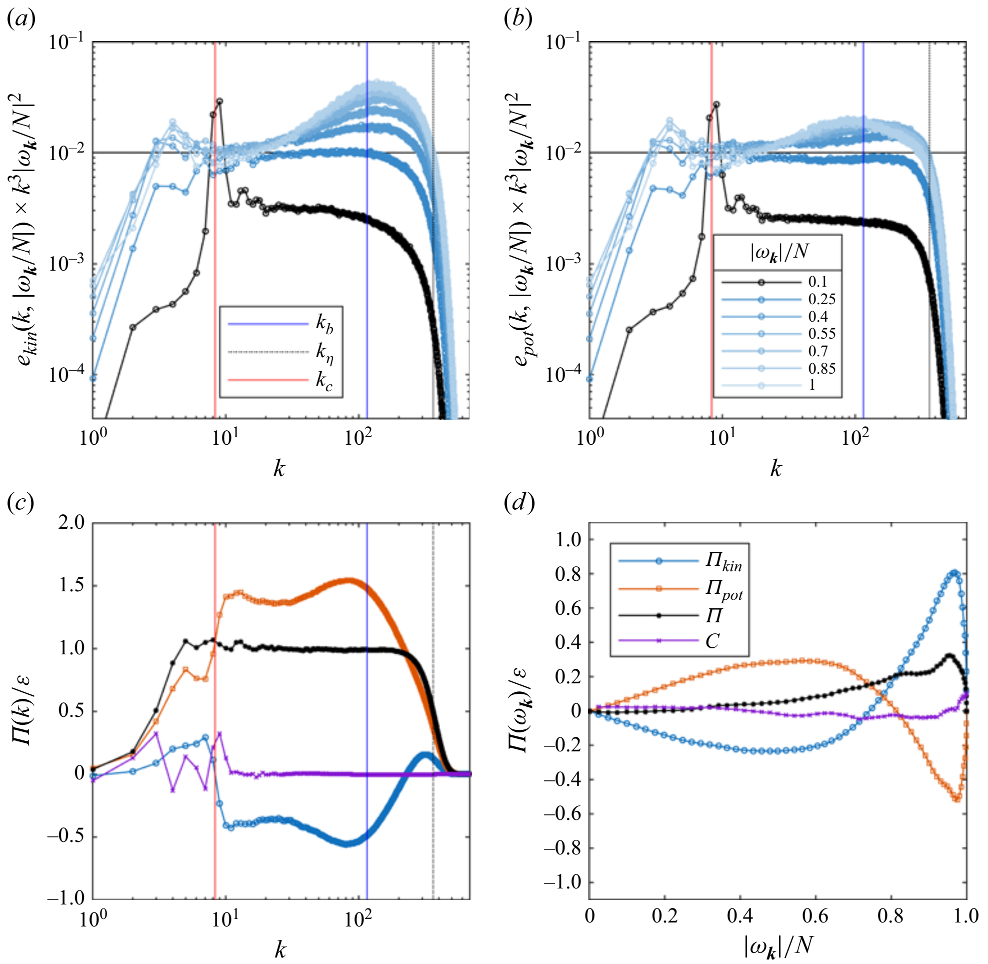

Figure 5. Energy spectra and energy transfers for the simulation in the strong nonlinear regime with $k_f/k_b = Fr = 0.026$ and $k_b/k_\eta = 0.32$. (*a*) Slices of the compensated kinetic energy spectrum and (*b*) slices of the compensated potential energy spectrum for different wave frequencies. (*c*) Normalised energy transfers (2.17) and conversion (2.19) as a function of k. (*d*) Normalised energy transfers (2.18) and conversion (2.20) as a function of $|\omega_{\boldsymbol{k}}|/N$. Legend in panel (*a*) is used for panels (*b*) and (*c*), legend in panel (*b*) is used for panel (*a*), and legend in panel (*d*) is used for panel (*c*).

peak at the critical wavevector $k \simeq k_c$ (3.10), corresponding to layering. It indicates that $k_c \propto Fr^{-3/5}$, obtained using weak wave turbulence theory in § 3, is relevant for strongly stratified flows beyond the weakly nonlinear regime. The potential energy spectrum, shown in panel (*b*), follows the same trends with a less pronounced bump at $k = k_b$.

In panel (*c*), we show the energy transfers (2.17), averaged over time in the steady state.

(i) For $k \lesssim k_c$, the transfers Π_{kin} and Π_{pot} have no clear behaviour, with a sharp transition around k_c.

(ii) For $k \in [k_c, k_b]$, the transfers have clear tendencies. Potential energy goes forward (to small scales) while converted to kinetic energy, and the kinetic energy goes backward (to large scale) and is converted back to potential energy. The total energy transfer equals the average injection rate ε. Interestingly, this picture is consistent with the energy cycle explained by Müller *et al.* (1986) (see figures 27 and 28 of this reference). This loop mechanism is different from that identified by Boffetta *et al.* (2011), which takes place in the isotropic range of turbulence (i.e. $k \in [k_O, k_\eta]$) when the velocity forcing is at small scales.

(iii) In the range $k \in [k_b, k_\eta]$, Π_{pot} decreases and Π_{kin} increases such that both are positive, and their sum is still ε.

(iv) At $k \simeq k_\eta$, Π_{kin} and Π_{pot} decrease to zero. The transfers are negligible only when $k \simeq k_d$ and it is tempting to interpret the range $k \in [k_\eta, k_d]$ as an 'intermittent' range. Yet, the smallness of this range does not allow it to be conclusive.

We see that the conversion rate (2.19) fluctuates for $k \leqslant k_c$, while it is close to zero for $k \gtrsim k_c$. It means that there is no significant net energy conversion at small scales. In panel (*d*), we show the energy transfers (2.18) as a function of $|\omega_{\boldsymbol{k}}|/N = |\cos\theta|$. Here, Π_{kin} and Π_{pot} are non-monotonous and have opposing trends. At low wave frequencies, the kinetic energy goes to smaller $\omega_{\boldsymbol{k}}$ and the potential energy to larger $\omega_{\boldsymbol{k}}$. It explains the layering observed in the vorticity field for slow waves at low Fr (figure 3*c*–*d*). The total energy transfer is positive for all wave frequencies meaning that the total energy transfer is towards higher $\omega_{\boldsymbol{k}}$. The conversion rate is close to zero at all wave frequencies, except for $|\omega/N| \simeq 1$, where $C > 0$, meaning that fast waves convert kinetic energy to potential energy in this simulation.

5.4. *Layering*

To explain the layering in our strongly stratified simulations, we use the empirical observation that the potential energy goes forward in wavenumber space and the kinetic energy goes backward. We further assume that the backward kinetic energy transfer stops at $k \simeq k_c$ due to the discreteness of the wave–wave interactions, so the energy accumulates at this scale. Since condition (3.8) is more easily broken at small wave frequencies, we expect the energy accumulation to be preferentially for small $\omega_{\boldsymbol{k}}$.

If the inverse energy transfers stop at $k \simeq k_c$, a mechanism must act against the accumulation of kinetic energy. Otherwise, simulations of 2-D stratified turbulence without shear modes would not reach a statistically steady state, as observed here and by Calpe Linares (2020). One possible mechanism is that the energy carried by the inverse kinetic transfers is converted to potential energy at $k \simeq k_c$. If k_c is in the inertial range, the energy budget (2.11) and (2.12) in steady state gives

$$\mathcal{C}(\boldsymbol{k}) = -\mathcal{T}_{kin}(\boldsymbol{k}) = \mathcal{T}_{pot}(\boldsymbol{k}) \tag{5.3}$$

for $\boldsymbol{k} = (k_x, k_z) \simeq (k_f, k_c)$. Using definitions (2.13) and (2.16), we obtain the order of magnitude estimates

$$C(\boldsymbol{k}) \sim k_x |\hat{b}_{\boldsymbol{k}}||\hat{\psi}_{\boldsymbol{k}}|, \quad \mathcal{T}_{kin} \sim k^2 k_x k_z |\hat{\psi}_{\boldsymbol{k}}|^3 \quad \text{and} \quad \mathcal{T}_{pot} \sim \frac{1}{N^2} k_x k_z |\hat{\psi}_{\boldsymbol{k}}||\hat{b}_{\boldsymbol{k}}|^2. \tag{5.4}$$

It follows that

$$|\hat{\psi}_{\boldsymbol{k}}| \sim \frac{N}{k_z^2} \quad \text{and} \quad |\hat{b}_{\boldsymbol{k}}| \sim \frac{N^2}{k_z}. \tag{5.5}$$

The large-scale flow velocity then scales as

$$U_L \sim |\partial_z \psi| \sim k_z |\hat{\psi}_{\boldsymbol{k}}| \sim \frac{N}{k_z} \sim U \frac{N}{U k_c} = U Fr^{-2/5}, \tag{5.6}$$

where we have used $k_z \simeq k_c$ and (3.10).

For shear modes, $k_x = 0$ and the conversion rate is $\mathcal{C}(\boldsymbol{k}) = 0$, so the kinetic energy accumulating at large scales cannot go back to small scales by conversion to potential energy. Consequently, if shear modes were included, we expect more kinetic energy at large scales, i.e. a stronger large-scale flow, when compared with the present simulations without shear modes. It may explain why strongly stratified simulations with shear modes take much longer to reach a steady state (Smith 2001; Smith & Waleffe 2002) (see also Brethouwer *et al.* 2007 and references therein). When shear modes are present, the steady state is reached after several instabilities (Caulfield 2021), leading to the increase of the layers' thickness and large-scale flow velocity (Remmel *et al.* 2014; Fitzgerald & Farrell 2018). Note that our reasoning implies that the vertical Froude number based on $L_z = 2\pi/k_c$ and U_L, namely $U_L/(NL_z)$, is of order unity. It is therefore consistent with earlier studies (Billant & Chomaz 2001; Brethouwer *et al.* 2007). For our simulations, where layering is present, $U_{rms} = \sqrt{2E_{kin}}$ is close to the large scale flow velocity U_L. We observe in figure 2(*b*) that U_{rms} follows the expected scaling (5.6). Therefore, our prediction gives a first-order estimate of the r.m.s. velocity of our simulations. Interestingly, the scaling (5.6) remains valid even if we force only buoyancy or velocity (Appendix).

In many studies, e.g. Billant & Chomaz (2001), Brethouwer *et al.* (2007), Augier *et al.* (2015), Calpe Linares (2020), Caulfield (2021), one uses the (turbulent) horizontal Froude number and the buoyancy Reynolds number which are respectively (Brethouwer *et al.* 2007)

$$F_h \equiv \frac{\varepsilon_{kin}}{NU_{rms}^2} \quad \text{and} \quad \mathcal{R} = \frac{\varepsilon_{kin}}{\nu N^2}, \tag{5.7}$$

where $n = 1$ and $\nu_n = \nu$ (standard viscosity and diffusivity), and ε_{kin} is the kinetic energy dissipation rate. Calpe Linares (2020) have extended these definitions to the hyperviscous case ($n \neq 1$):

$$F_h \equiv \frac{\varepsilon_{kin}}{NU_{rms}^2} \quad \text{and} \quad \mathcal{R}_n = \frac{\varepsilon_{kin} U_{rms}^{2n-2}}{\nu_n N^{2n}}. \tag{5.8}$$

Here, F_h represents the ratio between the large-scale flow overturning and buoyancy frequency, while $\mathcal{R}_n$ compares the ratio between vertical advection and vertical diffusion (see § 2.3 of Calpe Linares 2020). For $\mathcal{R}_n \lesssim 1$, vertical diffusion dominates. It is the viscosity-affected regime. The opposite case $\mathcal{R}_n \gg 1$ corresponds to the strongly stratified turbulence regime (Billant & Chomaz 2001; Brethouwer *et al.* 2007; Calpe Linares 2020). If we use the estimates $U_{rms} \propto U_L$ and $\varepsilon_{kin} \propto \varepsilon$, we can link F_h and $\mathcal{R}_n$ to Fr and k_b/k_η (3.13). We obtain

$$F_h \propto Fr^{9/5} \quad \text{and} \quad \mathcal{R}_n \propto Fr^{(22-12n)/15} \left(\frac{k_b}{k_\eta}\right)^{(2-6n)/3}. \tag{5.9}$$

Note that for standard viscosity, one has $\mathcal{R} = Fr^{2/3}(k_b/k_\eta)^{-4/3} = (k_\eta/k_O)^{4/3}$ so large $\mathcal{R}$ corresponds to flows with an isotropic inertial range between k_O and k_η (Brethouwer *et al.* 2007). From (5.9), we see that the condition for observing the strongly stratified turbulence regime ($\mathcal{R} \gg 1$) is different from the condition for observing the weak wave turbulence regime (3.14). The two regimes are therefore different. Also, there is a qualitative difference between standard viscosity ($n = 1$) and hyperviscosity ($n \geqslant 2$). To see it, let us consider a constant $k_b/k_\eta \gtrsim 1$. Then, for standard viscosity, $\mathcal{R}$ increases with *Fr*. In contrast, for hyperviscosity, $\mathcal{R}_n$ decreases with *Fr*. Therefore, a simulation with hyperviscosity and low Fr falls in the strongly stratified turbulence regime. Furthermore, a simulation with standard viscosity falls in the viscosity-affected regime.

5.5. *Verification of the weak wave turbulence prediction*

Weak wave turbulence means that weakly nonlinear waves carry most of the energy (Le Reun *et al.* 2017, 2018; Yokoyama & Takaoka 2019; Lam, Delache & Godeferd 2020). One can check it by looking at the spatiotemporal energy spectrum

$$e(\boldsymbol{k}, \omega) = \frac{k^2 \left|\hat{\psi}_{\boldsymbol{k}}(\omega)\right|^2}{2} + \frac{\left|\hat{b}_{\boldsymbol{k}}(\omega)\right|^2}{2N^2}, \tag{5.10}$$

where $\hat{\psi}_{\boldsymbol{k}}(\omega)$ and $\hat{b}_{\boldsymbol{k}}(\omega)$ are the Fourier transform in time of $\hat{\psi}_{\boldsymbol{k}}(t)$ and $\hat{b}_{\boldsymbol{k}}(t)$. Physically, $e(\boldsymbol{k}, \omega)$ is the energy density at wave vector $\boldsymbol{k}$ and temporal frequency ω. If the flow is of weakly nonlinear waves, we expect $e(\boldsymbol{k}, \omega) \neq 0$ only for $\omega \simeq \pm\omega_{\boldsymbol{k}}$. Otherwise, strong nonlinear interactions or other flow modes are important (Nazarenko 2011).

In figure 6, we show the spatiotemporal energy spectrum as a function of $\omega_{\boldsymbol{k}}$ and ω for four simulations, obtained after a straightforward summation over $\boldsymbol{k}$. To compute this spectrum, we use modes with $|\boldsymbol{k}| \leqslant M/4 < k_{max}$ to save computational time. Since these modes contain most of the energy, this truncation has little impact on the results. For weak stratification, the energy is not only on the linear dispersion relation curve, as shown in figure 6(*a*,*b*). For a simulation at higher stratification, shown in panel (*c*), we see that most of the energy is concentrated near the linear dispersion relation, meaning that this simulation is more likely to meet weak wave turbulence assumptions. We will use this simulation to compare the energy spectra with the theoretical prediction.

In figure 7(*a*,*b*), we show slices of the kinetic and potential energy spectra (5.2), averaged over time in the steady state, compensated by the weak wave turbulence prediction (1.1), for the simulation with $Fr = 0.026$ and $k_b/k_\eta = 1.2$. We see a good agreement between the theory and our DNS, except for low frequencies $\omega_{\boldsymbol{k}}/N$, where a spectral peak is present due to layering. Also, the potential energy spectrum decreases faster than the kinetic energy spectrum, particularly at high $\omega_{\boldsymbol{k}}/N$, because the potential energy is ‘taxed’ by the conversion to kinetic energy while transferred to small scales. We see in figure 7(*c*,*d*) that the energy transfers are similar to the simulation with smaller k_b/k_η (figure 5*c*,*d*), except that there is less inertial range. Additionally, we observe a peak of the conversion rate at $k \simeq k_c$ (panel *c*), indicating that kinetic energy converts to potential energy at this wavevector. To our knowledge, it is the first verification of the theoretical prediction for weak non-hydrostatic internal gravity wave turbulence. Interestingly, forcing only the buoyancy or the velocity does not deteriorate the agreement with the theoretical prediction, and the energy fluxes remain similar (Appendix).

5.6. *Doppler shift*

Keeping the stratification high and increasing the nonlinearity compared with the weak wave turbulence simulation, we see that the energy shifts away from the dispersion relation $\omega = \pm\omega_{\boldsymbol{k}}$ (figure 6*d*). This Doppler shift occurs in rotating and/or stratified flows due to the nonlinear interactions with the large-scale flow (see e.g. Campagne *et al.* 2015; Clark di Leoni & Mininni 2015; Lam *et al.* 2020). To quantify this Doppler shift, we compare the linear wave frequency with the empirical frequency,

$$\omega_{emp}(\omega_{\boldsymbol{k}}) = \sum_{\omega} \omega\, e(\omega_{\boldsymbol{k}}, \omega) \Bigg/ \sum_{\omega} e(\omega_{\boldsymbol{k}}, \omega). \tag{5.11}$$

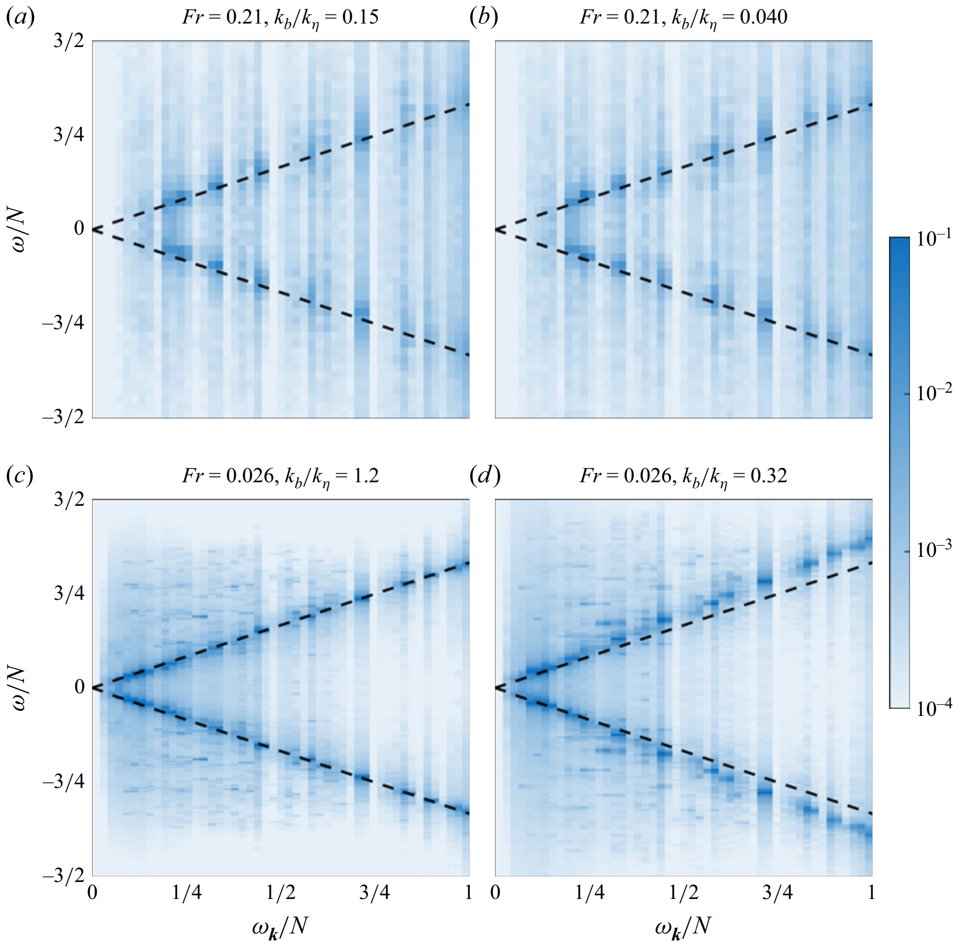

Figure 6. Spatiotemporal energy spectrum $e(\omega_{\boldsymbol{k}}, \omega)$ for four of our simulations. In all panels, the dashed lines correspond to the dispersion relation $\omega = \pm\omega_{\boldsymbol{k}}$.

In figure 8, we show ω_{emp} as a function of $\omega_{\boldsymbol{k}}$ for all our simulations. Panel (*a*) corresponds to weak stratification $Fr = 0.21$. In this case, ω_{emp}/N is close to unity for all wave frequencies, so energy is not on the linear dispersion relation. The empirical frequency depends weakly on k_b/k_η. In panel (*b*), for $Fr = 0.10$, ω_{emp} is closer to the wave dispersion relation for higher $\omega_{\boldsymbol{k}}$ and still has a weak dependence on k_b/k_η. In panel (*c*), for $Fr = 0.052$, ω_{emp} is close to $\omega_{\boldsymbol{k}}$ except at small wave frequencies. In panel (*d–f*), for $Fr \leqslant 0.026$, we observe different behaviour depending on k_b/k_η. For the highest k_b/k_η, ω_{emp} gets closer to $\omega_{\boldsymbol{k}}$ as Fr decreases. In contrast, for smallest k_b/k_η, we observe a significant shift in ω_{emp}. This Doppler shift is visible for three simulations: $(Fr = 0.026, k_b/k_\eta = 0.62)$, $(Fr = 0.026, k_b/k_\eta = 0.32)$ and $(Fr = 0.013, k_b/k_\eta = 1.2)$, shown in panels (*d*) and (*e*). It prevents us from using these simulations to compare weak wave turbulence predictions for the energy spectrum.

It is known that the Doppler shift appears when the sweeping frequency due to the large scale flow becomes larger than the linear frequency (see e.g. Clark di Leoni & Mininni 2015). In this case, the mean flow creates frequencies bigger than N that are undamped by

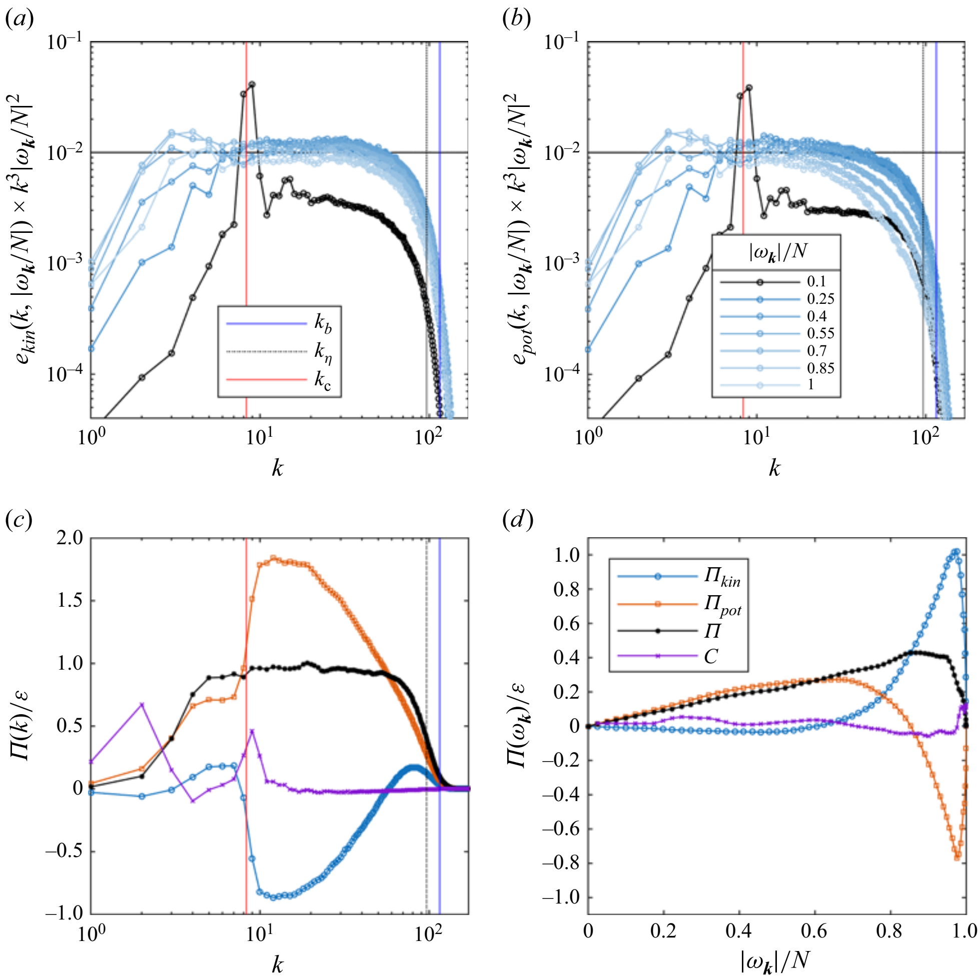

Figure 7. Energy spectra and energy transfers for the simulation with $Fr = 0.026$ and $k_b/k_\eta = 1.2$, in the weak wave turbulence regime. (*a*) Slices of the compensated kinetic energy spectrum and (*b*) slices of the compensated potential energy spectrum for different wave frequencies. (*c*) Normalised energy transfers (2.17) and conversion (2.19) as a function of k. (*d*) Normalised energy transfers (2.18) and conversion (2.20) as a function of $|\omega_{\mathbf{k}}|/N$. Legend in panel (*a*) is used for panels (*b*) and (*c*), legend in panel (*b*) is used for panel (*a*), and legend in panel (*d*) is used for panel (*c*).

viscosity. For our simulations, it yields to the condition

$$U_L k \gtrsim N. \tag{5.12}$$

To satisfy this condition in the inertial range, i.e. for $k \lesssim k_\eta$, it requires

$$U Fr^{-2/5} k_\eta \gtrsim \alpha N \quad \Rightarrow \quad \frac{k_b}{k_\eta} \lesssim \frac{1}{\alpha} Fr^{-2/5}, \tag{5.13}$$

where we have used (5.6) and α is an undetermined numerical constant. In figure 2(*a*), we show the line given by condition (5.13) with $\alpha = 4$, which is estimated from numerical results. The simulations affected by the Doppler shift are for low Fr and satisfy (5.13).

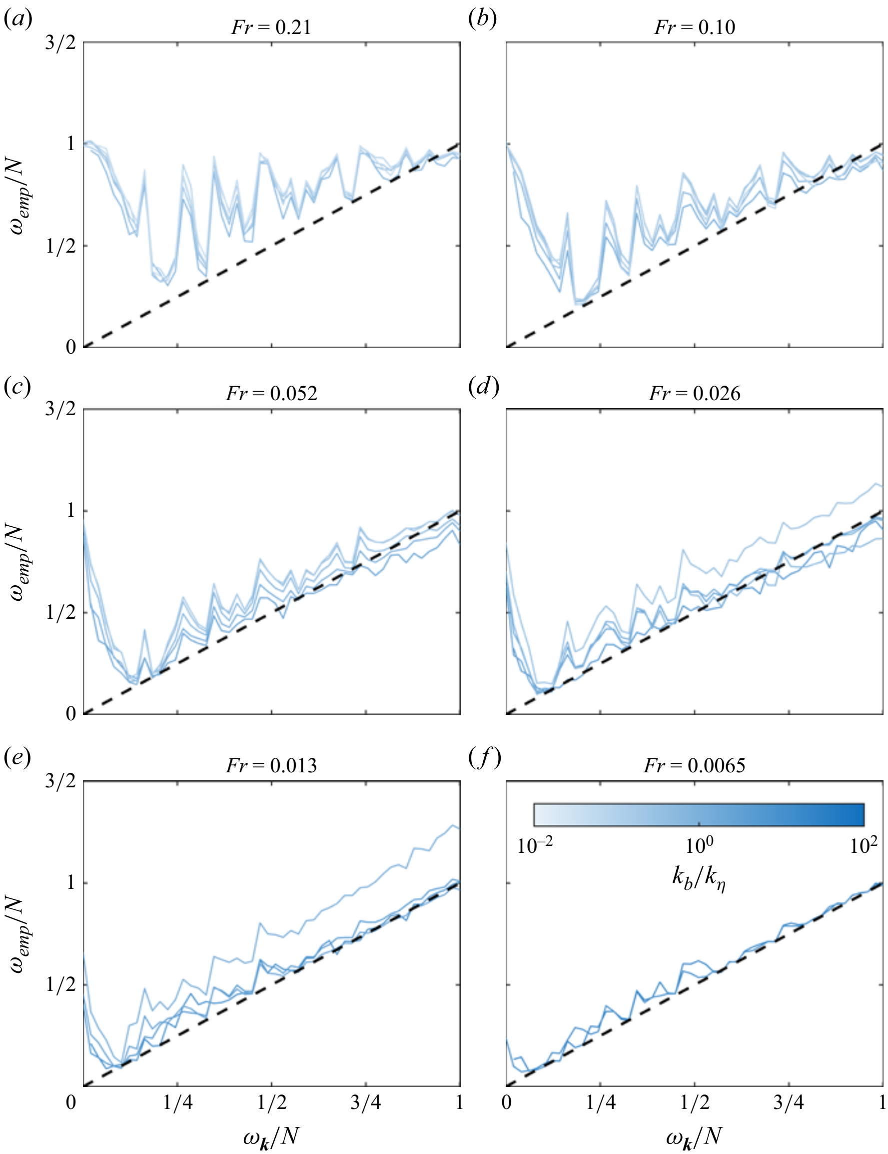

Figure 8. Empirical frequency (5.11) versus the wave frequency $\omega_{\boldsymbol{k}}$ for all our simulations. In all panels, the dashed line indicates $\omega_{emp} = \omega_{\boldsymbol{k}}$.

6. Conclusions and discussions

We performed direct numerical simulations of 2-D stratified turbulence without shear modes (also called vertically sheared horizontal flows). In the weak wave turbulence regime, we verified the theoretical predictions outside the hydrostatic limit (Shavit *et al.* 2025). The energy spectrum agrees with the theory except for low wave frequencies. Yet, our simulations are subject to layering – an accumulation of energy in slow waves – which perturbs the theoretical predictions. This layering also occurs outside weakly nonlinear regimes, as observed in many previous studies (Smith & Waleffe 2002; Laval *et al.* 2003; Waite 2011; Remmel *et al.* 2014; Fitzgerald & Farrell 2018; Calpe Linares 2020).

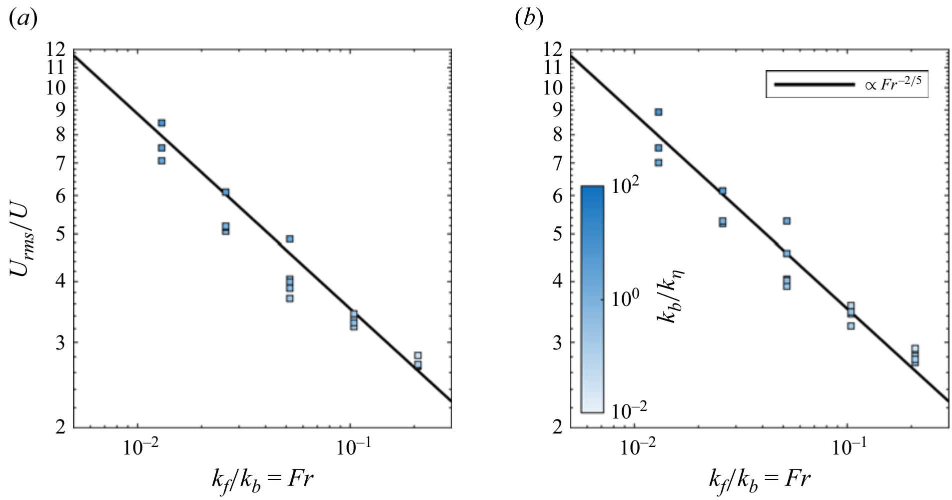

Figure 9. Ratio between the r.m.s. velocity U_{rms} and the typical velocity fluctuation due to the forcing $U = (\varepsilon/k_f)^{1/3}$ as a function of *Fr* for all simulations with (*a*) buoyancy forcing and (*b*) velocity forcing.

We explain the layering using: (i) the empirical observation that potential energy goes to small scales and kinetic energy goes to large scales; (ii) discreteness of the wave–wave interactions at large scales, typical of weakly nonlinear wave systems (Nazarenko 2011), attenuates the kinetic energy transfer at the largest scales; (iii) potential and kinetic energy budgets in statistically steady state. It allows us to obtain scaling laws for the layers' thickness L_z and the large-scale velocity U_L, using only the input parameters of the simulations. These predictions agree with our simulations, even outside the weakly nonlinear regime. It is also consistent with the idea that the flow selects L_z and U_L such that the vertical Froude number $U_L/(NL_z)$ is of order unity (Billant & Chomaz 2001). For strongly nonlinear–strongly stratified simulations, we observe that the measured wave frequency is impacted by a Doppler shift, commonly observed in stratified and rotating flows (Campagne *et al.* 2015; Clark di Leoni & Mininni 2015; Lam *et al.* 2020).

Two-dimensional stratified turbulence with shear modes and 3-D stratified turbulence are naturally more complex than the idealised simulations presented in this study. Indeed, other instabilities usually occur in stratified turbulence (Caulfield 2021). Yet, we expect our order of magnitude to be relevant for discussing some transitions of strongly stratified turbulence. In particular, the estimate $k_c = 2\pi/L_z \propto k_f Fr^{-3/5}$ may help to explain the emergence of layering in realistic flows and the discrepancies between simulations/experiments employing different set-ups. It is tempting to apply our argument to rotating flows for explaining the formation of vertical vortices as well. By analogy, $L_h = 2\pi/k_c$ would correspond to the radius of nearly vertical columnar flows with $k_c \propto k_f Ro^{-3/5}$, $Ro = k_f U/(2\varOmega)$ the Rossby number and $\varOmega$ the rotation rate. Importantly, we have used hyperviscosity in our simulations. Therefore, the applicability of these results to flows with standard viscosity remains an important topic for future inquiry.

To observe weak wave turbulence of internal waves, one must limit the large-scale flow, the size of which is determined by the threshold for discrete wave turbulence (Nazarenko 2011). It can be done by adding large-scale damping (Le Reun *et al.* 2017; Brunet *et al.* 2020), or by using a random forcing over the all discrete turbulence range $k \lesssim k_c$. Another way of preventing the formation of the large scale would be to use a large aspect ratio so the large-scale flow cannot exist in the simulation box or the container. Interestingly,

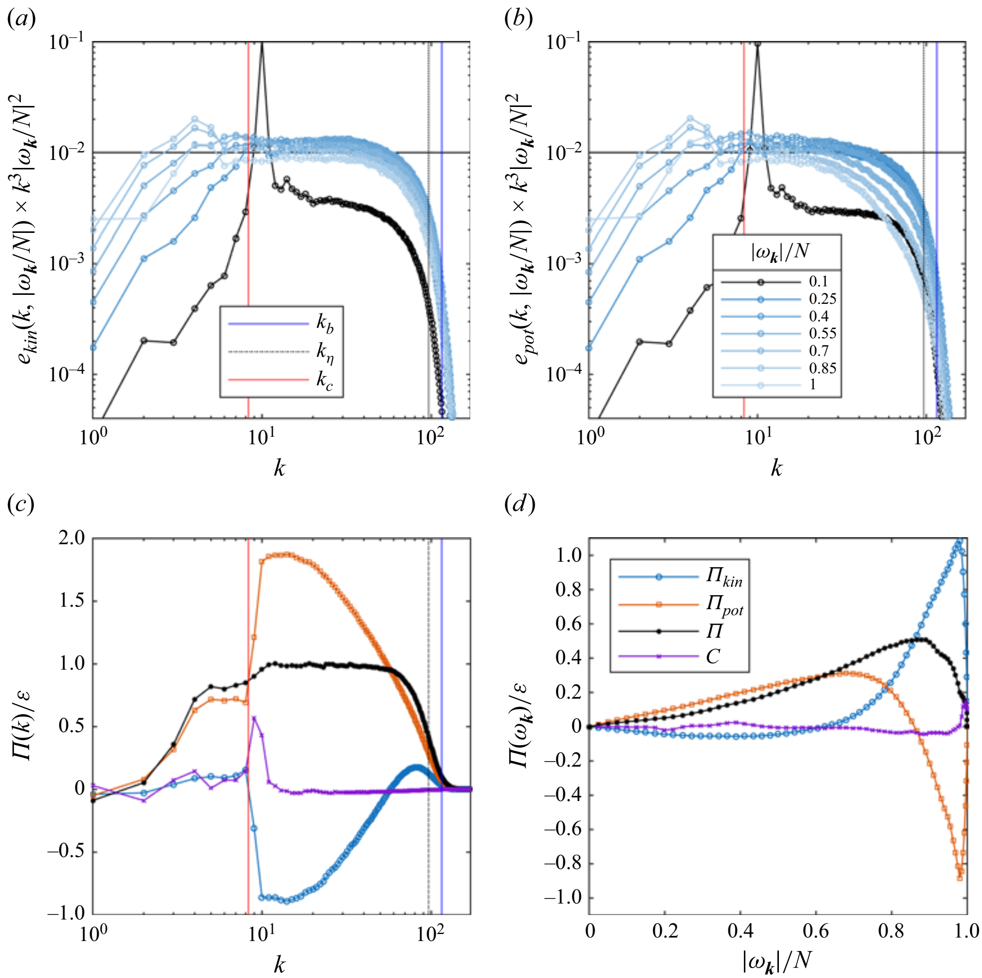

Figure 10. Energy spectra and energy transfers for the simulation with buoyancy forcing, and $Fr = 0.026$ and $k_b/k_\eta = 1.2$, in the weak wave turbulence regime. Legend is the same as in figure 7.

considering an asymptotic limit of the Navier–Stokes equations, van Kan & Alexakis (2020, 2022) identified transitions to large-scale flow formations for critical values of the aspect ratio. Yet, as explained by the authors, their asymptotic is different from weak wave turbulence and is unlikely to be directly related to the present work.

Acknowledgements. We thank G. Krstulovic for providing the structure for the code used in this work together with endless advice; O. Bühler, S. Nazarenko, J. Shatah, G. Falkovich, P. Augier, N. Mordant, P. Billant and C. Caulfield for fruitful discussions. We are grateful to three anonymous reviewers for their insightful comments, which significantly enhanced the quality of this work.

Funding. This work was supported by the Simons Foundation and the Simons Collaboration on Wave Turbulence. The numerical study was made possible thanks to New York University's Greene computing cluster facility. M.S. acknowledges additional financial support from the Schmidt Futures Foundation. We used AI for language polishing.

Declaration of interests. The authors report no conflict of interest.

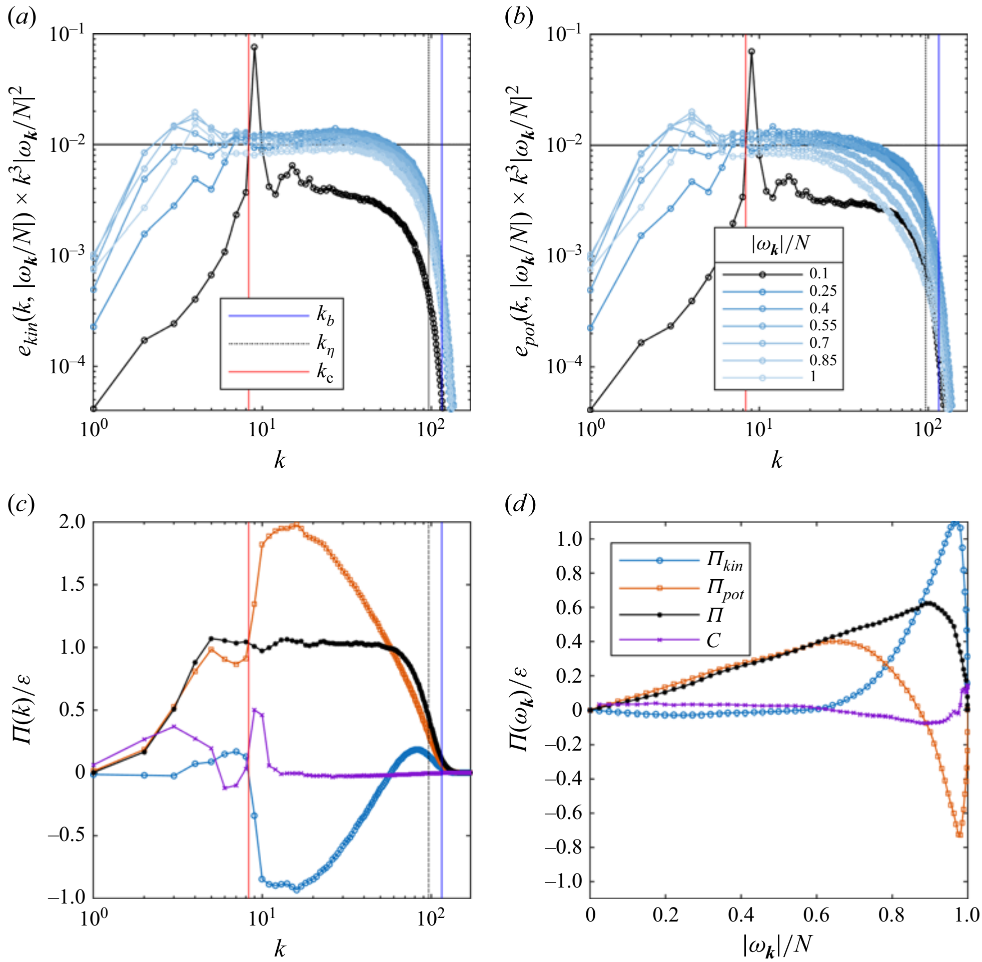

Figure 11. Energy spectra and energy transfers for the simulation with velocity forcing, and $Fr = 0.026$ and $k_b/k_\eta = 1.2$, in the weak wave turbulence regime. Legend is the same as in figure 7.

Data availability statement. The data that support the findings of this study can be reproduced using the information given in this manuscript. The authors can provide simulation outputs upon reasonable request.

Author contributions. Both authors conducted this study, performed the simulations and wrote the manuscript.

Appendix. Simulations with buoyancy or velocity forcing

We have run other simulations employing the same set-up (see § 4) and average energy injection rate still equal to $\varepsilon = 10^{-3}$, but with buoyancy forcing ($\hat{f}_{\psi,\boldsymbol{k}} = 0$) and velocity forcing ($\hat{f}_{b,\boldsymbol{k}} = 0$). In figure 9, we show the r.m.s. velocity as a function of Fr for different k_b/k_η. For both buoyancy (panel a) and velocity (panel b) forcings, we observe the same trend $U_{rms} \propto U Fr^{-2/5}$ (5.6). It shows that this scaling is not affected by the quantity we force in our strongly stratified simulations.

In figures 10 and 11, we show spectral energy budgets for simulations in the weak wave turbulence regime and respectively buoyancy and velocity forcing. We observe that the energy spectra (panels *a* and *b*), and energy transfers and conversion (panels *c* and *d*) are very similar with buoyancy forcing (figure 10), velocity forcing (figure 11) and mixed forcing (figure 7).

In particular, we find a good agreement with the theoretical prediction (1.1) for the three forcings. Also, the direct potential energy transfer, inverse kinetic energy transfer and conversion peak at $k \simeq k_c$ are the same (panel *c*). Therefore, the energy pathway at $k \geqslant k_c$ is the same for the three forcings. What changes is the conversion rate at wavevectors $k \leqslant k_c$. In the weak wave turbulence regime, it is close to zero for buoyancy forcing (figure 10*c*) and positive for kinetic energy forcing (figure 11*c*). We also note that the peaks in the energy spectra appear at a slightly larger value of $k > k_c$ for the simulation with buoyancy forcing (figure 10). It indicates that the factor *c*, used to define the critical wavevector k_c (3.10), could depend on the forcing mechanism.

References

Alexakis, A. & Biferale, L. 2018 Cascades and transitions in turbulent flows. *Phys. Rep.* **767–769**, 1–101.

Andrews, D.G., Holton, J.R. & Leovy, C.B. 1987 *Middle Atmosphere Dynamics. International Geophysics*, vol. 40, Elsevier Science.

Augier, P., Billant, P. & Chomaz, J.-M. 2015 Stratified turbulence forced with columnar dipoles: numerical study. *J. Fluid Mech.* **769**, 403–443.

Balmforth, N.J., Smith, L., Stefan, G. & Young, W.R. 1998 Dynamics of interfaces and layers in a stratified turbulent fluid. *J. Fluid Mech.* **355**, 329–358.

Billant, P. & Chomaz, J.-M. 2000*a* Experimental evidence for a new instability of a vertical columnar vortex pair in a strongly stratified fluid. *J. Fluid Mech.* **418**, 167–188.

Billant, P. & Chomaz, J.-M. 2000*b* Theoretical analysis of the zigzag instability of a vertical columnar vortex pair in a strongly stratified fluid. *J. Fluid Mech.* **419**, 29–63.

Billant, P. & Chomaz, J.-M. 2001 Self-similarity of strongly stratified inviscid flows. *Phys. Fluids* **13** (6), 1645–1651.

Boffetta, G., De Lillo, F., Mazzino, A. & Musacchio, S. 2011 A flux loop mechanism in two-dimensional stratified turbulence. *Europhys. Lett.* **95** (3), 34001.

Bourouiba, L. 2008 Discreteness and resolution effects in rapidly rotating turbulence. *Phys. Rev. E* **78**, 056309.

Brethouwer, G., Billant, P., Lindborg, E. & Chomaz, J.-M. 2007 Scaling analysis and simulation of strongly stratified turbulent flows. *J. Fluid Mech.* **585**, 343–368.

Brunet, M., Gallet, B. & Cortet, P.-P. 2020 Shortcut to geostrophy in wave-driven rotating turbulence: the quartetic instability. *Phys. Rev. Lett.* **124** (12), 124501.

Buckmaster, T., Germain, P., Hani, Z. & Shatah, J. 2021 Onset of the wave turbulence description of the longtime behavior of the nonlinear schrödinger equation. *Invent. Math.* **225**, 787–855.

Bühler, O. 2014 *Waves and Mean Flows*. Cambridge University Press.

Caillol, P. & Zeitlin, V. 2000 Kinetic equations and stationary energy spectra of weakly nonlinear internal gravity waves. *Dyn. Atmos. Oceans* **32** (2), 81–112.

Calpe Linares, M. 2020 Numerical study of 2-D stratified turbulence forced by internal gravity waves. PhD thesis, Université Grenoble Alpes, France.

Campagne, A., Gallet, B., Moisy, F. & Cortet, P.-P. 2015 Disentangling inertial waves from eddy turbulence in a forced rotating-turbulence experiment. *Phys. Rev. E* **91** (4), 043016.

Caulfield, C.P. 2021 Layering, instabilities, and mixing in turbulent stratified flows. *Annu. Rev. Fluid Mech.* **53** (2021), 113–145.

Dematteis, G., Le Boyer, A., Pollmann, F., Polzin, K.L., Alford, M.H., Whalen, C.B. & Lvov, Y.V. 2024 Interacting internal waves explain global patterns of interior ocean mixing. *Nat. Commun.* **15** (1), 7468.

Dematteis, G. & Lvov, Y.V. 2021 Downscale energy fluxes in scale-invariant oceanic internal wave turbulence. *J. Fluid Mech.* **915**, A129.

Falcon, E. & Mordant, N. 2022 Experiments in surface gravity–capillary wave turbulence. *Annu. Rev. Fluid Mech.* **54**, 1–25.

Fitzgerald, J.G. & Farrell, B.F. 2018 Statistical state dynamics of vertically sheared horizontal flows in two-dimensional stratified turbulence. *J. Fluid Mech.* **854**, 544–590.

Galtier, S. 2022 *Physics of Wave Turbulence*. Cambridge University Press.

Garrett, C. & Munk, W. 1979 Internal waves in the ocean. *Annu. Rev. Fluid Mech.* **11** (1), 339–369.

Hasselmann, K. 1966 Feynman diagrams and interaction rules of wave-wave scattering processes. *Rev. Geophys.* **4** (1), 1–32.

Howard, L.N. 1961 Note on a paper of John W. Miles. *J. Fluid Mech.* **10** (4), 509–512.

Howland, C.J., Taylor, J.R. & Caulfield, C.P. 2020 Mixing in forced stratified turbulence and its dependence on large-scale forcing. *J. Fluid Mech.* **898**, A7.

van Kan, A. & Alexakis, A. 2020 Critical transition in fast-rotating turbulence within highly elongated domains. *J. Fluid Mech.* **899**, A33.

van Kan, A. & Alexakis, A. 2022 Energy cascades in rapidly rotating and stratified turbulence within elongated domains. *J. Fluid Mech.* **933**, A11.

Labarre, V., Augier, P., Krstulovic, G. & Nazarenko, S. 2024*a* Internal gravity waves in stratified flows with and without vortical modes. *Phys. Rev. Fluids* **9**, 024604.

Labarre, V., Lanchon, N., Cortet, P.-P., Krstulovic, G. & Nazarenko, S. 2024*b* On the kinetics of internal gravity waves beyond the hydrostatic regime. *J. Fluid Mech.* **998**, A17.

Lam, H., Delache, A. & Godeferd, F.S. 2020 Partitioning waves and eddies in stably stratified turbulence. *Atmosphere* **11** (4), 1–29.

Lanchon, N. & Cortet, P.-P. 2023 Energy spectra of nonlocal internal gravity wave turbulence. *Phys. Rev. Lett.* **131**, 264001.

Lanchon, N., Mora, D.O., Monsalve, E. & Cortet, P.-P. 2023 Internal wave turbulence in a stratified fluid with and without eigenmodes of the experimental domain. *Phys. Rev. Fluids* **8** (5), 054802.

Laval, J.-P., McWilliams, J.C. & Dubrulle, B. 2003 Forced stratified turbulence: Successive transitions with Reynolds number. *Phys. Rev. E* **68**, 036308.

Le Bars, M. 2023 Wave turbulence in geophysical flows. *J. Fluid Mech.* **962**, F1.

Le Reun, T., Favier, B., Barker, A.J. & Le Bars, M. 2017 Inertial wave turbulence driven by elliptical instability. *Phys. Rev. Lett.* **119**, 034502.

Le Reun, T., Favier, B. & Le Bars, M. 2018 Parametric instability and wave turbulence driven by tidal excitation of internal waves. *J. Fluid Mech.* **840**, 498–529.

Clark di Leoni, P. & Mininni, P.D. 2015 Absorption of waves by large-scale winds in stratified turbulence. *Phys. Rev. E* **91**, 033015.

L'vov, V.S. & Nazarenko, S. 2010 Discrete and mesoscopic regimes of finite-size wave turbulence. *Phys. Rev. E* **82**, 056322.

Lvov, Y. & Tabak, E.G. 2004 A Hamiltonian formulation for long internal waves. *Phys. D: Nonlinear Phenom.* **195** (1), 106–122.

Lvov, Y.V., Polzin, K.L., Tabak, E.G. & Yokoyama, N. 2010 Oceanic internal-wave field: theory of scale-invariant spectra. *J. Phys. Oceanogr.* **40** (12), 2605–2623.

Lvov, Y.V., Polzin, K.L. & Yokoyama, N. 2012 Resonant and near-resonant internal wave interactions. *J. Phys. Oceanogr.* **42** (5), 669–691.

Lvov, Y.V. & Tabak, E.G. 2001 Hamiltonian formalism and the Garrett–Munk spectrum of internal waves in the ocean. *Phys. Rev. Lett.* **87** (16), 168501.

MacKinnon, J.A., *et al.* 2017 Climate process team on internal wave–driven ocean mixing. *Bull. Am. Meteorol. Soc.* **98** (11), 2429–2454.

McComas, C.H. & Bretherton, F.P. 1977 Resonant interaction of oceanic internal waves. *J. Geophys. Res.* **82** (9), 1397–1412.

McLachlan, R.I. & Quispel, G.R.W. 2002 Splitting methods. *Acta Numerica* **11**, 341–434.

Miles, J.W. 1961 On the stability of heterogeneous shear flows. *J. Fluid Mech.* **10** (4), 496–508.

Müller, P., Holloway, G., Henyey, F. & Pomphrey, N. 1986 Nonlinear interactions among internal gravity waves. *Rev. Geophys.* **24** (3), 493–536.

Nazarenko, S. 2011 *Wave Turbulence. Lecture Notes in Physics*, vol. 1. Springer Berlin Heidelberg.

Newell, A.C. & Rumpf, B. 2011 Wave turbulence. *Annu. Rev. Fluid Mech.* **43** (1), 59–78.

Olbers, D.J. 1976 Nonlinear energy transfer and the energy balance of the internal wave field in the deep ocean. *J. Fluid Mech.* **74** (2), 375–399.

Pelinovsky, E.N. & Raevsky, M.A. 1977 Weak turbulence of the internal waves of the ocean. *Atmos. Ocean Phys. Izvestija* **13**, 187–193.

Petropoulos, N., Mashayek, A. & Caulfield, C.-C.P. 2023 Turbulent disruption of density staircases in stratified shear flows. *J. Fluid Mech.* **961**, A30.

Phillips, O.M. 1972 Turbulence in a strongly stratified fluid—is it unstable? *Deep Sea Res. Oceanogr. Abstracts* **19** (1), 79–81.

Polzin, K.L., Garabato, N., Alberto, C., Huussen, T.N., Sloyan, B.M. & Waterman, S. 2014 Finescale parameterizations of turbulent dissipation. *J. Geophys. Res.: Oceans* **119** (2), 1383–1419.

https://doi.org/10.1017/jfm.2026.11329 Published online by Cambridge University Press

REMMEL, M., SUKHATME, J. & SMITH, L.M. 2014 Nonlinear gravity-wave interactions in stratified turbulence. *Theor. Comput. Fluid Dyn.* **28** (2), 131–145.

RILEY, J.J. & LINDBORG, E. 2008 Stratified turbulence: a possible interpretation of some geophysical turbulence measurements. *J. Atmos. Sci.* **65** (7), 2416–2424.

RODDA, C., SAVARO, C., DAVIS, G., RENEUVE, J., AUGIER, P., SOMMERIA, J., VALRAN, T., VIBOUD, S. & MORDANT, N. 2022 Experimental observations of internal wave turbulence transition in a stratified fluid. *Phys. Rev. Fluids* **7**, 094802.

ROGERS, T.M., LIN, D.N.C., MCELWAINE, J.N. & LAU, H.H.B. 2013 Internal gravity waves in massive stars: angular momentum transport. *Astrophys. J.* **772** (1), 21.

SCOTT, J.F. & CAMBON, C. 2024 Evolution of weak, homogeneous turbulence with rotation and stratification. *J. Fluid Mech.* **979**, A17.

SHAVIT, M., BÜHLER, O. & SHATAH, J. 2024 Sign-indefinite invariants shape turbulent cascades. *Phys. Rev. Lett.* **133**, 014001.

SHAVIT, M., BÜHLER, O. & SHATAH, J. 2025 Turbulent spectrum of 2-D internal gravity waves. *Phys. Rev. Lett.* **134**, 054101.

SHAVIT, M., BÜHLER, O. & SHATAH, J. 2026 Wave turbulence of inertia–gravity waves: a theory for the oceanic spectrum. arXiv preprint arXiv: 2601.01476.

SMITH, L. 2001 Numerical study of two-dimensional stratified turbulence. *Contemp. Maths* **283**, 91.

SMITH, L.M. & WALEFFE, F. 2002 Generation of slow large scales in forced rotating stratified turbulence. *J. Fluid Mech.* **451**, 145–168.

SMITH, S.G.L. & YOUNG, W.R. 2003 Tidal conversion at a very steep ridge. *J. Fluid Mech.* **495**, 175–191.

TAYLOR, J.R. & ZHOU, Q. 2017 A multi-parameter criterion for layer formation in a stratified shear flow using sorted buoyancy coordinates. *J. Fluid Mech.* **823**, R5.

VALLIS, G.K. 2017 *Atmospheric and Oceanic Fluid Dynamics*. Cambridge University Press.

WAITE, M.L. 2011 Stratified turbulence at the buoyancy scale. *Phys. Fluids* **23** (6), 066602.

WHALEN, C.B., DE LAVERGNE, C., NAVEIRA GARABATO, A.C., KLYMAK, J.M., MACKINNON, J.A. & SHEEN, K.L. 2020 Internal wave-driven mixing: governing processes and consequences for climate. *Nat. Rev. Earth Environ.* **1** (11), 606–621.

YOKOYAMA, N. & TAKAOKA, M. 2019 Energy-based analysis and anisotropic spectral distribution of internal gravity waves in strongly stratified turbulence. *Phys. Rev. Fluids* **4**, 104602.

ZAKHAROV, V.E., L'VOV, V.S. & FALKOVICH, G. 1992 *Kolmogorov Spectra of Turbulence I. Springer Series in Nonlinear Dynamics*, vol. 1. Springer.

ZHU, Y., SEMISALOV, B., KRSTULOVIC, G. & NAZARENKO, S. 2022 Testing wave turbulence theory for the Gross–Pitaevskii system. *Phys. Rev. E* **106** (1), 014205.